

# PROBABILITY DISTRIBUTION FUNCTIONS OF SUNSPOT MAGNETIC FLUX

TAKASHI SAKURAI<sup>1,2</sup> AND SHIN TORIUMI<sup>3</sup>

<sup>1</sup>*National Astronomical Observatory of Japan, 2-21-1 Osawa, Mitaka, Tokyo 181-8588, Japan*

<sup>2</sup>*Earth-Life Science Institute, Tokyo Institute of Technology, 2-12-1 Ookayama, Meguro, Tokyo 152-8550, Japan*

<sup>3</sup>*Institute of Space and Astronautical Science, Japan Aerospace Exploration Agency, Sagami-hara, Kanagawa 229-5210, Japan*

(Received April 12, 2022; Revised November 4, 2022; Accepted November 14, 2022)

Submitted to ApJ

## ABSTRACT

We have investigated the probability distributions of sunspot area and magnetic flux by using the data from Royal Greenwich Observatory and USAF/NOAA. We have constructed a sample of 2995 regions with maximum-development areas  $\geq 500$  MSH (millionths of solar hemisphere), covering 146.7 years (1874–2020). The data were fitted by a power-law distribution and four two-parameter distributions (tapered power-law, gamma, lognormal, and Weibull distributions). The power-law model was unfavorable compared to the four models in terms of AIC, and was not acceptable by the classical Kolmogorov-Smirnov test. The lognormal and Weibull distributions were excluded because their behavior extended to smaller regions ( $S \ll 500$  MSH) do not connect to the previously published results. Therefore, our choices were tapered power-law and gamma distributions. The power-law portion of the tapered power-law and gamma distributions was found to have a power exponent of 1.35–1.9. Due to the exponential fall-off of these distributions, the expected frequencies of large sunspots are low. The largest sunspot group observed had an area of 6132 MSH, and the frequency of sunspots larger than  $10^4$  MSH was estimated to be every  $3 - 8 \times 10^4$  years. We also have estimated the distributions of the Sun-as-a-star total sunspot areas. The largest total area covered by sunspots in the record was 1.67 % of the visible disk, and can be up to 2.7 % by artificially increasing the lifetimes of large sunspots in an area evolution model. These values are still smaller than those found on active Sun-like stars.

*Keywords:* Solar activity (1475), Solar magnetic fields (1503), Solar photosphere (1518), Sunspots (1653), Starspots (1572)

## 1. INTRODUCTION

Sunspots represent a variety of magnetic activities of the Sun (Solanki 2003; van Driel-Gesztelyi & Green 2015). It is thought that the dynamo mechanism in the solar interior intensifies and transports magnetic flux to the surface and eventually builds up active regions (ARs) including sunspots (Parker 1955). Even after four centuries of continuous observations, the sunspots still maintain important positions in the investigation of the dynamo processes in the Sun.

Another importance of sunspots is their close relationship with flare activity (Priest & Forbes 2002; Shibata & Magara 2011; Toriumi & Wang 2019). Statistical investigations have revealed that greater flares emanate from larger ARs (Sammis et al. 2000). This may be natural since larger ARs harbor more magnetic flux and thus more magnetic free energy available. The largest observed sunspot group since the late nineteenth century was the one in 1947 April, the largest area of which was 6132 MSH (millionths of solar hemisphere;  $1 \text{ MSH} = 3.04 \times 10^6 \text{ km}^2$ ) or about 1.2 % of the visible solar disk (Figure 1). While this region was not flare-active, another giant sunspot in 1946 July caused larger flares with geomagnetic disturbances (Toriumi et al. 2017). The formation mechanism of such great ARs is an interesting issue to be resolved.

The existence of spots is also known for other stars (Berdyugina 2005; Strassmeier 2009). One of the largest starspots reported thus far was from a K0 giant XX Tri (HD 12545), which covered about 20% of the entire stellar surface (Strassmeier 1999). It was found that even solar-type stars producing the so-called superflares (Schaefer et al. 2000; Maehara et al. 2012) host starspots much larger than the solar ones (up to  $\sim 10\%$  of the stellar hemisphere; Notsu et al. 2013, 2015). Therefore, the discussion of superflares on the Sun is closely related to the question of the production of super-large sunspots.

The key quantity we study in this paper is the probability distribution function of the area  $S$  or magnetic flux  $\Phi$  of sunspots. Bogdan et al. (1988) analyzed the Mt. Wilson white-light observations (1917–1982) of sunspots and showed that the sunspot umbral areas [1.5–141 MSH; the corresponding total sunspot areas would be about five times of these (Solanki 2003)] follow the lognormal distribution. Hathaway & Choudhary (2008) obtained the same conclusion using the data from the Royal Greenwich Observatory (RGO) and the United States Air Force [USAF; data were compiled and distributed by the National Oceanic and Atmospheric Administration (NOAA)] covering the period 1874–2007 (sunspot areas larger than 35 MSH). Baumann & Solanki (2005) studied the RGO data (1874–1976) of sunspots with areas  $\geq 60$  MSH, by making a distinction between a snapshot distribution and a maximum area distribution; the former is derived from daily data (e.g. Bogdan et al. 1988; Hathaway & Choudhary 2008) while the latter is derived by following the time evolution of individual regions and by recording their maximum areas. They found that the two distributions are fitted by lognormal distributions that have similar parameter values. This property was also mentioned in Hathaway & Choudhary (2008).

The fall-off of the lognormal distribution toward small sunspot areas may be because smaller magnetic concentrations tend to lose their darkness and eventually end up with small flux tubes brighter than the surroundings (Zwaan 1987). On the other hand, the fall-off of the lognormal distribution toward large sunspot areas was not paid much attention. In this context, Gopalswamy (2018, Figure 6) applied the Weibull distribution (Weibull 1939), which is often used to describe the failure rates of industrial products, to the RGO and USAF/NOAA sunspot area data (maximum-area distribution).

The tail of the observed distribution was fitted equally well by a power law and Weibull, and the latter gives more rapid decline and less frequent appearance of extremely large regions.

Since sunspots are made (i.e. obtain their darkness) because of their magnetic fields by inhibition of convective heat transport (e.g. Spruit 1977), the probability distribution of magnetic flux in magnetic structures (including sunspots) is an equally important quantity. Harvey & Zwaan (1993) analyzed the magnetograms obtained at the US National Solar Observatory at Kitt Peak (NSO/Kitt Peak) in the period 1975–1986 and derived the distribution of magnetic flux at the maximum development of individual active regions. For regions with areas larger than 121 MSH the magnetic flux emergence rate was approximated by a power law. Schrijver & Harvey (1994) gave a more specific fitting equation with a power-law exponent of about 2.0 [probability  $\propto \Phi^{-\alpha}$  with  $\alpha \simeq 2$ ; in this article  $\alpha(> 0)$  is called the power-law exponent]. Hagenaar et al. (2003) investigated the emergence rates of ephemeral regions (small-scale bipolar magnetic field patches) using the data from the Michelson Doppler Imager onboard the Solar and Heliospheric Observatory (SOHO/MDI; Scherrer et al. 1995) taken between 1996 and 2001. They found that the distribution looked like an exponential function. Thornton & Parnell (2011) analyzed the emergence rates of small-scale magnetic field patches using the data from the Solar Optical Telescope onboard the Hinode satellite (Hinode/SOT; Tsuneta et al. 2008) and obtained a power-law formula extending all the way up to the active-region scales, with a power-law exponent of 2.69. All of these results are summarized and discussed later in Section 5 and in Figure 7. Balmaceda et al. (2009), Muñoz-Jaramillo et al. (2015), and Mandal et al. (2020) give detailed accounts on the issues on sunspot area calibration. Muñoz-Jaramillo et al. (2015) also tried several models (power law, lognormal, Weibull, exponential, and their combinations) to fit the area distributions.

In this paper, we will use the data from RGO (1874–1976) and USAF/NOAA (1977 - 2020) and derive the maximum areas of individual regions (Section 2). Recurrent regions are counted only once when their areas reach the maximum. In order to compare these with magnetic field observations of active regions and smaller magnetic patches, we will convert the sunspot areas to magnetic flux values (Section 2.2). Our primary interest here is whether the sunspot area or magnetic flux distribution extends to large values in the form of a power law or is tapered off, to address whether the Sun may have super-large sunspots like in super-flare stars. Therefore, we limit the data of sunspots with areas 500 MSH or larger, and try to fit the data with five kinds of distribution functions; power law, tapered power law, gamma, lognormal, and Weibull distributions (Section 3). Statistical examinations (Section 4) and comparison with previously published results (Section 5) show preference on the tapered power law and gamma distributions. Using the obtained results, we can predict the expected frequencies of super-large sunspots. In Section 6, we will adopt a simple time-evolution model of sunspot areas and examine the effects of assumptions we made in our analysis. Particularly we can estimate the snapshot (instantaneous) distribution of sunspot areas (Section 6.3) and also a distribution of Sun-as-a-star total sunspot areas (Section 6.4), and will discuss their implications on super-large stellar spots (Section 7).

## 2. DATA

### 2.1. Data Sources

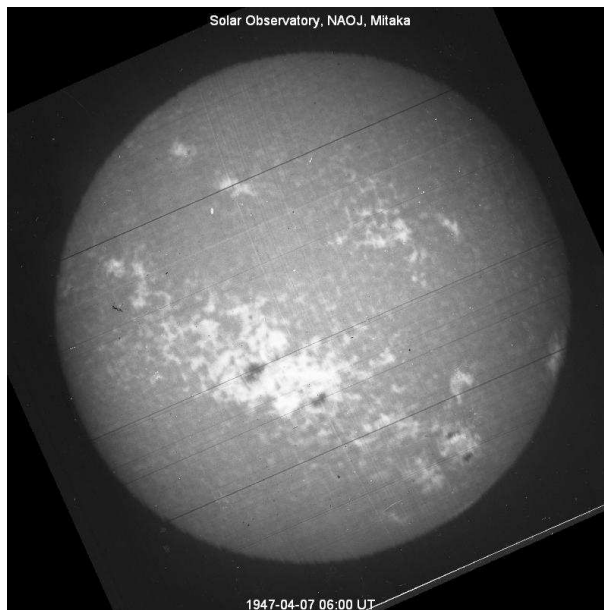


**Figure 1.** Ca K-line spectroheliogram of 1947 April 7 taken at Mitaka, Tokyo; celestial north is up, west to the right. The big active region near the disk center is RGO region 14886 which showed a foreshortening-corrected area of 6132 MSH, the largest on the record, on April 8.

The Greenwich Photoheliographic Results (GPR) in PDF are available through the SAO/NASA Astrophysics Data System (ADS), NOAA<sup>1</sup>, and the UK Solar System Data Center<sup>2</sup>. The digitized data of sunspot areas recorded in GPR (1874 April – 1976) are provided at several sites<sup>3,4,5</sup>. Systematic observation and data collection of sunspots at RGO started on 1874 April 17 (Christie 1907). The correction for foreshortening was explained to have been applied to regions of angular distance within 80° from the disk center (Spencer Jones 1955), but regions beyond were occasionally recorded. From these data sets we have picked up regions whose foreshortening-corrected maximum-development areas ( $S_{\text{md}}$ ) are 500 MSH or larger. If the corrected area  $S$  of a region was monotonically increasing or decreasing on the visible hemisphere, we defined the maximum value of  $S$  as the maximum-development area  $S_{\text{md}}$ , although the true maximum took place on the back-side of the Sun. The effects of this assumption will be estimated in Section 6. For recurrent regions, we only retained the maximum  $S$  over all their disk passages because they were regarded as generated from the identical magnetic flux tubes generated by the dynamo. For this we had to identify recurrent regions, and such lists are available in Maunder (1909) (1874–1906), and “Catalogue of Recurrent Groups of Sun Spots” (1910–1955), “Ledger I: Recurrent Groups” (1916–1955), and “General Catalog of Groups of Sunspots” (1956–1976) sections of GPR.

The data after the cessation of RGO solar observations in 1976 were taken from USAF/NOAA (1977–2020)<sup>5</sup>. As no convenient lists are available to identify recurrent regions, we did this manually by relying on the following data: H $\alpha$  synoptic charts in Solar Geophysical Data (SGD)<sup>6</sup> (1977–1989),

<sup>1</sup> [ftp://ftp.ngdc.noaa.gov/STP/SOLAR\\_DATA/SOLAR\\_OBSERVATION/GREENWICH/](ftp://ftp.ngdc.noaa.gov/STP/SOLAR_DATA/SOLAR_OBSERVATION/GREENWICH/)

<sup>2</sup> <http://www.ukssdc.ac.uk/wdcc1/RGOPHR/>

<sup>3</sup> [ftp://ftp.ngdc.noaa.gov/STP/SOLAR\\_DATA/SUNSPOT\\_REGIONS/Greenwich/](ftp://ftp.ngdc.noaa.gov/STP/SOLAR_DATA/SUNSPOT_REGIONS/Greenwich/)

<sup>4</sup> <http://fenyi.solarobs.csfk.mta.hu/GPR/>

<sup>5</sup> <http://solarcyclescience.com/activerregions.html>

<sup>6</sup> [ftp://ftp.ngdc.noaa.gov/STP/SOLAR\\_DATA/SGD\\_PDFversion/](ftp://ftp.ngdc.noaa.gov/STP/SOLAR_DATA/SGD_PDFversion/)

NOAA Report of Solar and Geophysical Activity (RSGA)<sup>7</sup> (1990–2000), NOAA Weekly Preliminary Report and Forecast of SGD (Weekly PRF)<sup>7</sup> (2001–2009), and Debrecen Photoheliographic Data (DPD)<sup>8</sup> (2010–2020). We have picked up regions with the foreshortening-corrected maximum-development area exceeding  $500/1.20 = 415$  MSH (see below). The distribution of angular distances from the disk center did not show a clear decline toward the limb and continued up to  $90^\circ$ , implying that the foreshortening correction was applied to all the USAF/NOAA data.

In the end we have selected 2995 regions, 2175 from RGO and 820 from USAF/NOAA data, covering 1874 April to 2020 December, 146.7 years (Table 1). Before obtaining the final list, we have removed 363 and 101 regions from RGO and USAF/NOAA data as they were members of recurrent regions. The data fully cover 13 solar cycles, from Cycle 12 (1878 December – 1890 March) to Cycle 24 (2008 December – 2019 December).

**Table 1.** Data

No.	Date	Data source	Region number	RGO area [MSH]	Original area <sup>a</sup> [MSH]	Magnetic flux [Mx]
1	1947-04-08	RGO	14886	6132.0	6132	3.18E+23
2	1946-02-07	RGO	14417	5202.0	5202	2.69E+23
3	1951-05-19	RGO	16763	4865.0	4865	2.51E+23
4	1946-07-29	RGO	14585	4720.0	4720	2.44E+23
5	1989-03-18	NOAA	5395	4320.0	3600	2.23E+23
6	1982-06-15	NOAA	3776	3720.0	3100	1.92E+23
7	1926-01-19	RGO	9861	3716.0	3716	1.92E+23
8	1989-09-04	NOAA	5669	3696.0	3080	1.91E+23
9	1990-11-19	NOAA	6368	3696.0	3080	1.91E+23
10	1938-01-21	RGO	12673	3627.0	3627	1.87e+23

<sup>a</sup>: NOAA area before converted to the RGO scale.

NOTE—Table 1 is published in its entirety in the machine-readable format. Only the top ten regions are shown here to explain the format of the table.

## 2.2. Sunspot Area vs. Magnetic Flux

In order to relate the sunspot area and the total radial unsigned magnetic flux (including the flux outside of the sunspots), we used the SHARP data series (Bobra et al. 2014) of the Helioseismic and Magnetic Imager (HMI; Scherrer et al. 2012; Schou et al. 2012) aboard the Solar Dynamics Observatory (SDO; Pesnell et al. 2012). We picked up all available CEA (cylindrical equal area)-remapped definitive SHARP data from 2010 to 2015 that contained the sunspots of NOAA areas  $\geq 500$  MSH within  $45^\circ$  from the disk center. In total, 137 patches were collected (one patch per

<sup>7</sup> <ftp://ftp.swpc.noaa.gov/pub/warehouse/>

<sup>8</sup> <http://fenyi.solarobs.csfk.mta.hu/DPD/>

region per day). From each patch, we carefully eliminated magnetic concentrations that were not related to the target ARs.

In order to evaluate the total unsigned magnetic flux in maxwell (Mx) from the list of the sunspot areas, we investigated the relation between the sunspot area,  $S_{\text{HMI}}$ , and the total unsigned radial flux,  $\Phi_{\text{HMI}}$ , which can also be calculated from the SHARP data. Note that we measured the total flux only within the smooth bounding curve of the SHARP data to minimize the possibility of including flux that was not related to the target AR and to reduce the noise effect. Figure 2(a) shows a scatter plot between  $S_{\text{HMI}}$  and  $\Phi_{\text{HMI}}$ . From the least-squares fitting to this double logarithmic plot, we obtained the relation between the two parameters,

$$\begin{aligned} \log(\Phi_{\text{HMI}} [\text{Mx}]) = & (1.010 \pm 0.132) \times \log(S_{\text{HMI}} [\text{MSH}]) \\ & + (19.676 \pm 0.400), \end{aligned} \quad (1)$$

(log means  $\log_{10}$ ; for natural logarithm we use “ln” in this paper) where we assumed that both  $\Phi_{\text{HMI}}$  and  $S_{\text{HMI}}$  have errors (Deming 1943; Press et al. 1992). The obtained conversion equation shows that the total flux is almost linearly related to the sunspot area,  $\Phi/S \simeq 1660$  gauss (AR flux/sunspot area for  $S \simeq 500$  MSH). For comparison, Schrijver & Harvey (1994) derived AR flux/AR area  $\simeq 150$  gauss.

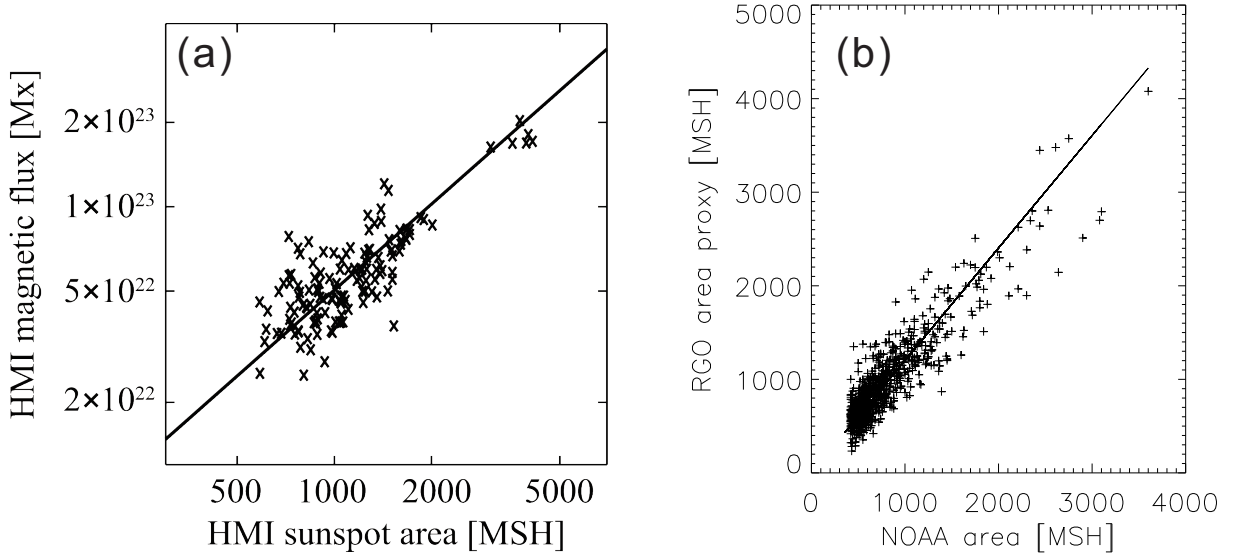


**Figure 2.** (a) Scatter plot between sunspot areas and total unsigned magnetic fluxes in ARs, both taken from the SHARP data, with the linear fitting to the log-log plot: see Equation (1). (b) Comparison of sunspot areas reported by NOAA vs. the database of Mandal et al. (2020) that reproduces the RGO area scale. The number of samples is 762. The solid line shows the regression line [Equation (2)]

### 2.3. Sunspot Area Calibration

It is known that the USAF/NOAA sunspot areas,  $S_{\text{NOAA}}$ , are systematically smaller than the RGO ones,  $S_{\text{RGO}}$ . In general, the multiplication of the USAF/NOAA values by 1.4–1.5 gives better agreement with the RGO values (e.g., Fligge & Solanki 1997; Hathaway et al. 2002; Balmaceda et al.



2009; Hathaway 2015). However, Foukal (2014) showed that the inconsistency between the RGO and USAF/NOAA data sets was mainly due to very small sunspots ( $\lesssim 2$  MSH) and that the areas for  $> 300$  MSH equalized. In order to examine if the NOAA records of larger ARs show systematically smaller values, we used the database developed by Mandal et al. (2020) which was calibrated to give the same area scale as RGO and was extended to 2021<sup>9</sup>. Among our 820 NOAA regions we excluded 58 regions which we suspect that NOAA and Mandal et al. (2020) used different group definitions.

Figure 2(b) shows the comparison of 762 regions. We found that mean and standard deviation of the area ratios,  $S_{\text{RGO}}/S_{\text{NOAA}}$ , are  $1.20 \pm 0.01$ . Therefore, we simply assumed that the RGO data sets provide reliable values and the NOAA values are converted by

$$S = S_{\text{HMI}} = S_{\text{RGO}} = 1.20 \times S_{\text{NOAA}}. \quad (2)$$

Mandal et al. (2020) obtained the conversion factor of 1.48, but the method of comparison is different; they compared daily data while our data are region-wise, maximum-development areas. We have also made the analysis adopting a conversion factor of about 1.4 and found basically the same results, although detailed numerical values changed.

Under the assumption of Equation (2), we then applied Equation (1) to the maximum-development sunspot areas  $S_{\text{md}}$  of both RGO and USAF/NOAA to generate the database on the maximum-development magnetic flux  $\Phi_{\text{md}}$ . A 500 MSH sunspot corresponds to a magnetic flux of  $2.53 \times 10^{22}$  Mx. The largest sunspot so far, RGO 14886 in 1947 April (6132 MSH), is estimated to have a total flux of  $3.18 \times 10^{23}$  Mx. Flux estimations of modern events such as NOAA 9169, 9393, 10486, and 12192 showed good agreements with the independent measurements by, e.g., Tian & Alexander (2008), Smyrli et al. (2010), Criscuoli et al. (2009), Zhang et al. (2010), and Sun et al. (2015).

### 3. STATISTICAL ANALYSIS

#### 3.1. Definitions

Our data are made of  $N_s = 2995$  values of sunspot magnetic flux at their maximum development,  $\Phi_{\text{md},i}$  ( $i = 1, 2, \dots, N_s$ ) (subscript “s” is meant for “sources” or “source flux tubes”). In the following we simply designate  $\Phi_{\text{md}}$  as  $\Phi$  unless we have to distinguish between maximum-development values and other cases. The minimum value of  $\Phi_i$ ’s is  $\Phi_1 = 2.53 \times 10^{22}$  Mx, corresponding to an area of 500 MSH. As a histogram representation of data depends on how one defines the data bins (Clauset et al. 2009), we will work on the complementary cumulative distribution function [CCDF, represented by  $F(\Phi)$ ] shown in Figure 3a, which is uniquely defined in terms of a given observational data set [Equation (A4)]. CCDF is a decreasing function of its argument while the cumulative distribution function (CDF) is an increasing function; therefore, the usage of CCDF is intuitively more straightforward in comparing with the probability distribution function that is also a decreasing function of its argument in the present case.

The slope (or derivative) of CCDF is the usual probability distribution function [PDF, represented by  $P(\Phi)$ ], but here we introduce dimensional parameters and define the flux emergence rate  $f(\Phi)$  in units of regions  $\text{Mx}^{-1}\text{Mm}^{-2}\text{d}^{-1}$  as (Figure 3b)

$$f(\Phi) = P(\Phi) \frac{N_s}{AT}, \quad P(\Phi) = -\frac{dF(\Phi)}{d\Phi}, \quad (3)$$

<sup>9</sup> [http://www2.mps.mpg.de/projects/sun-climate/data/indivi\\_group\\_area\\_1874\\_2021\\_Mandal.txt](http://www2.mps.mpg.de/projects/sun-climate/data/indivi_group_area_1874_2021_Mandal.txt)

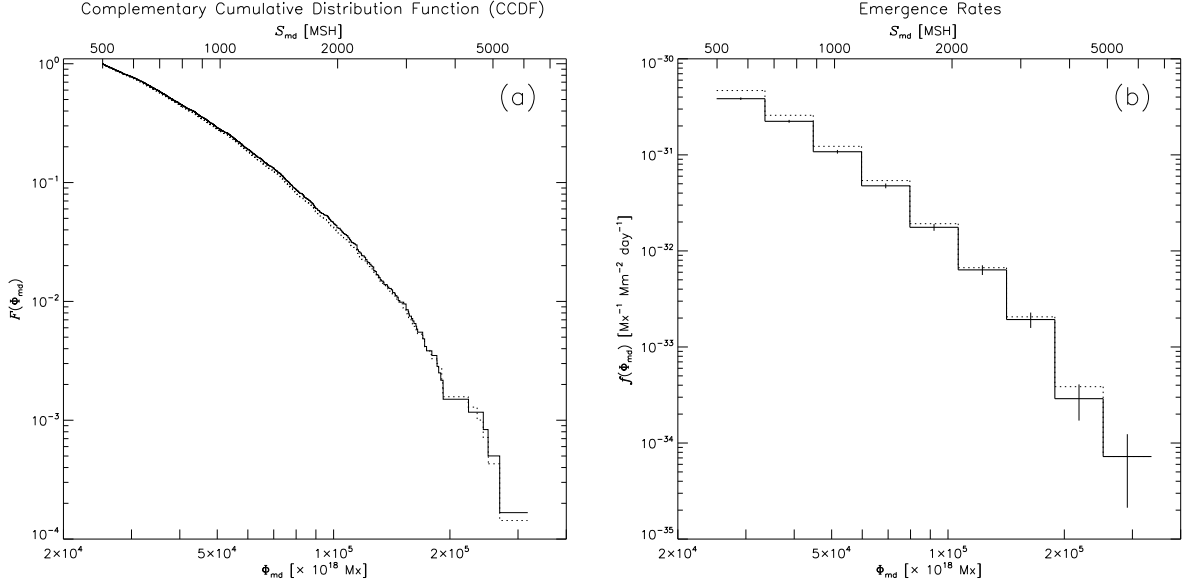


**Figure 3.** (a) The complimentary cumulative distribution function (CCDF)  $F(\Phi)$  of magnetic flux  $\Phi_{\text{md}}$  [Mx] of large sunspot regions ( $S_{\text{md}} \geq 500$  MSH) at their maximum development, observed from 1874 April to the end of 2020 (146.7 years). The top horizontal axis shows the corresponding sunspot areas. The dotted curve represents the distribution when recurrent regions not at their maximum development are all counted. (b) A histogram representing the distribution function  $f(\Phi_{\text{md}})$  of emergence rates of magnetic flux  $\Phi_{\text{md}}$  of large sunspot regions, per bin width, unit area in  $\text{Mm}^2$ , and day. The bin width is  $\Delta \log \Phi_{\text{md}} = 0.125$ . Vertical bars indicate the  $\sqrt{N}$  uncertainty of  $N$  regions contained in each bin (the last bin only contains two regions). The dotted histogram represents the distribution when recurrent regions not at their maximum development are all counted.

where  $A$  stands for the area of observation (the full Sun, e.g.  $6.2 \times 10^6 \text{ Mm}^2$  in Sections 4 and 5 and the hemisphere in Sections 6.3) and  $T = 146.7 \text{ years} = 5.36 \times 10^4 \text{ days}$ . A histogram is generated showing  $f(\Phi_j) = N_j / (AT\Delta\Phi_j)$ , where  $j$  stands for the bin number, and  $N_j$  is the number of sunspot groups with flux values ranging from  $\Phi_j$  to  $\Phi_j + \Delta\Phi_j$ . The flux bins are taken equi-distant in  $\log \Phi$  ( $\Delta \log \Phi = \text{constant} = 0.125$ ), so that  $\Delta\Phi_j = \Phi_j \ln(10) \Delta(\log \Phi_j)$ . The quantity  $N_s = \sum_j N_j$  is explicitly used when we compare the observed histogram with a theoretical distribution function  $P$ .

In Figures 3a and 3b, the solid curves are from the maximum development areas while the dotted curves show the cases when we did not exclude the recurrent regions other than their maximum area development. We can expect that a larger region may appear multiple times at smaller areas and increase the counts at lower bins. The effect of not excluding recurrent regions is to slightly steepen the slope of the distribution.

### 3.2. Models and Fitting Procedures

In this paper we will try to fit the observed data set  $\Phi_i$  by

- (1) a power-law distribution (parameter:  $\alpha_1$ ),
- (2) a tapered power-law distribution (parameters:  $\alpha_2, \beta_2$ ),
- (3) a truncated gamma distribution (parameters:  $\alpha_3, \beta_3$ ),



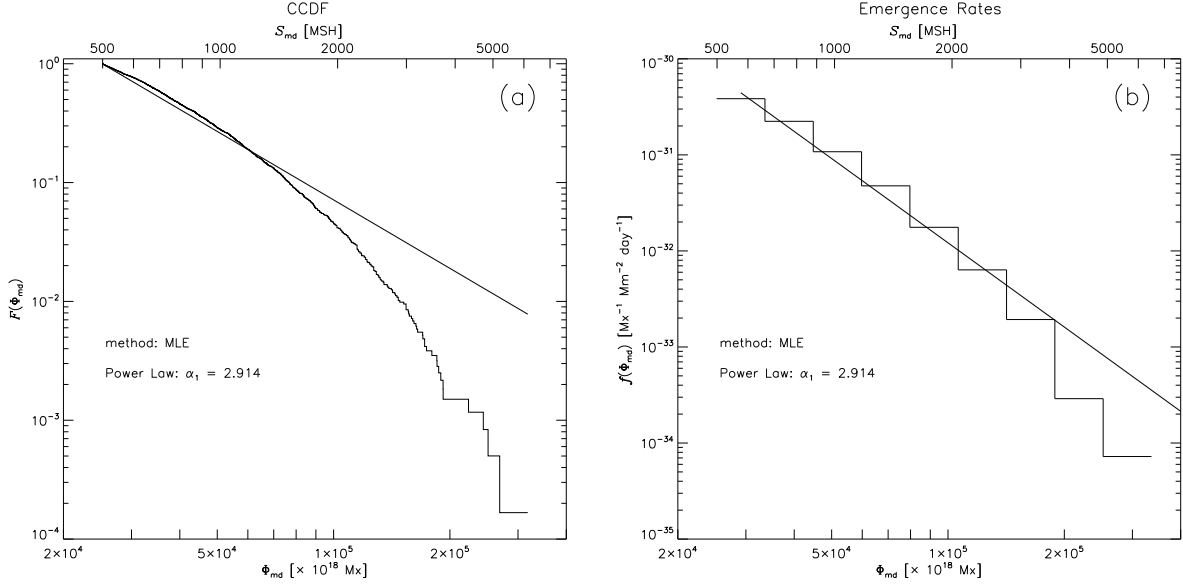


**Figure 4.** (a) An MLE power-law fit (straight line) to the complimentary cumulative distribution function of magnetic flux  $F(\Phi)$ . (b) The power-law fit of panel (a) for  $F(\Phi)$  is converted to the probability distribution function  $f(\Phi)$  and is overplotted on the histogram of the data.

(4) a truncated lognormal distribution (parameters:  $\mu, \sigma$ ), and

(5) a truncated Weibull distribution (parameters:  $k, \beta_5$ ).

A tapered power-law distribution (also called the Pareto distribution of the third kind (Johnson et al. 1994) in contrast to the original Pareto distribution which is a pure power law) has a CCDF that is a product of a power law and an exponential function. A gamma distribution has a PDF that is a product of a power law and an exponential function, and its CCDF is represented in terms of the gamma function. These have been used to describe the distribution functions of earthquake magnitudes (e.g. Kagan 2002; Serra & Corral 2017), in comparison with the power-law distribution which is named the Gutenberg-Richter relation in seismology (e.g. Utsu 1999).

The power-law distribution is a one-parameter model while the other four are two-parameter models. Models (1), (2), and (3) have a power-law component with the exponent  $\alpha_1$ ,  $\alpha_2$ , and  $\alpha_3$ , respectively. Models (2), (3), and (5) have an exponential component whose decay coefficients are represented by  $\beta_2$ ,  $\beta_3$ , and  $\beta_5$ . The best-fit parameter values can be given systematically by the maximum-likelihood estimator (MLE), by maximizing the log-likelihood (LLH),

$$\text{LLH} = \sum \ln(P(\Phi_i)). \quad (4)$$

The definitions of these five distributions and their MLE solutions are given in Appendix A.

Whether one model is more superior to the others can be assessed by comparing the AIC values (Akaike 1974),

$$\text{AIC} = -2 \times \max(\text{LLH}) + 2K, \quad (5)$$

where  $K$  is the number of parameters ( $K = 1$  or  $2$  in our analysis). (In another often-used criteria, Bayesian information criteria or BIC,  $K \ln n$  ( $n$  is the sample size) is used instead of  $2K$ ;

**Table 2.** Derived parameters and 1- $\sigma$  error ranges

Model	Method	Parameter values and errors		$\Delta\text{AIC}^a$	$\sqrt{N_s}$ KS <sup>b</sup>	KS prob. <sup>c</sup>	KSr P-value <sup>d</sup>
Power law							
	MLE	$\alpha_1 = 2.914 \pm 0.035$		184.6	4.14	$< 10^{-6}$	0.019
Tapered power law							
	MLE	$\alpha_2 = 1.808 \pm 0.091$	$\beta_2 = 0.669 \pm 0.056$	2.79	1.059	0.210	0.290
	KSr=min	$\alpha_2 = 1.886 \pm 0.153$	$\beta_2 = 0.614 \pm 0.083$	3.77	1.211	0.105	0.444
Gamma							
	MLE	$\alpha_3 = 1.358 \pm 0.138$	$\beta_3 = 0.591 \pm 0.057$	1.51	0.989	0.279	0.458
	KSr=min	$\alpha_3 = 1.450 \pm 0.224$	$\beta_3 = 0.547 \pm 0.083$	2.11	1.08	0.195	0.665
Lognormal							
	MLE	$\mu = -0.300 \pm 0.099$	$\sigma = 0.777 \pm 0.035$	1.55	0.630	0.817	0.414
	KSr=min	$\mu = -0.157 \pm 0.188$	$\sigma = 0.728 \pm 0.061$	4.27	1.075	0.196	0.490
Weibull							
	MLE	$k = 0.625 \pm 0.044$	$\beta_5 = 2.278 \pm 0.217$	0.00	0.827	0.497	0.911
	KSr=min	$k = 0.629 \pm 0.068$	$\beta_5 = 2.270 \pm 0.396$	0.06	0.868	0.434	0.850

<sup>a</sup>: Relative AIC values with respect to the minimum value of all the AIC values.

<sup>b</sup>: Kolmogorov-Smirnov statistic KS derived from the observed data and the assumed model, multiplied by  $\sqrt{N_s}$ .

<sup>c</sup>: Theoretical probability that the KS metric shows values larger than the observed KS metric.

<sup>d</sup>: Probability based on the simulation runs that the simulated KSr values are larger than the observed KSr value.

Burnham & Anderson (2002).) By increasing the number of parameters, the fitting becomes better and LLH increases. However, the introduction of more parameters is not justified if AIC does not decrease. If the AIC value of one model is smaller than the AIC of the other by 9–11 or more, the former model is regarded better than the latter (Burnham et al. 2011).

AIC is a relative measure, and it is possible that the model preferred by AIC still gives a poor fit. Whether the fitting by one model is not satisfactory and should be rejected can be estimated by evaluating a statistical measure that quantifies the difference between the observed and modeled CCDFs and by comparing that measure with a theoretical threshold (Stephens 1970, 2016). Here we use the Kolmogorov-Smirnov statistic KS defined by Equation (B36). For a large-enough  $N_s$ , the probability for the observed  $\sqrt{N_s}$  KS value or larger to be obtained is theoretically given as a function (Kolmogorov-Smirnov function) which has relatively weak dependence on  $N_s$ . Alternatively we can utilize simulation runs to estimate the probability (see below).

Once the parameter values are obtained, we can estimate their error ranges using the parametric bootstrap method (Efron & Tibshirani 1993; Burnham & Anderson 2002) as follows.

- (1) Generate  $N_s$  sets of uniform random variables  $y_i$ ,  $i = 1, 2, \dots, N_s$  ( $0 \leq y_i \leq 1$ ).

- (2) Find  $\Phi_i$  such that  $F(\Phi_i) = y_i$ .
- (3) For the data set  $\Phi_i$  ( $i = 1, 2, \dots, N_s$ ), obtain the MLE solutions for the parameters and the KS statistic.
- (4) Repeat (1)–(3)  $m$  times; then the distributions of the parameter values and the KS statistic are obtained.
- (5) Evaluate the  $1-\sigma$  width of these distributions and adopt them as the error ranges of the parameters.
- (6) For the KS statistic, if the number of cases where the KS values exceed the observed value  $\text{KS}_{\text{obs}}$  is  $m'$ , then  $m'/m$  gives the probability (P-value) that such a value of  $\text{KS}_{\text{obs}}$  is obtained under the assumed model.

The  $1-\sigma$  values defined in step (5) scale basically as  $1/\sqrt{N_s}$  and do not depend on  $m$  if it is taken sufficiently large (we used  $m = 10^5$ ).

The procedure described above has some points to consider. First, the MLE solution is not intended to geometrically fit a model CCDF to the observed CCDF. Particularly, it does not care much about the fitting at the tail, because the MLE solution is mostly determined by data points of highest density, i.e. near to the lower end of the distribution. A more geometrically-favorable solution may be obtained by, say, minimizing directly the KS statistic. Second, the KS statistic is not sensitive to misfitting at the lower and upper ends of the distribution, because by definition both the observed and model CCDF match (taking the values of 0 or 1) at the ends. It is known that the contributions to KS roughly scales as  $1/\sqrt{F(1-F)}$  (Anderson & Darling 1952), and Clauset et al. (2009) suggested to use a modified form of the KS statistic by dividing its components by  $1/\sqrt{F(1-F)}$  to enhance the sensitivity of the test at both ends. Here we introduce a KSr (revised KS) statistic defined by Equation (B37), by dividing only by  $1/\sqrt{F}$  to enhance the sensitivity at the tail.

In summary, we will apply two methods.

- Method 1: Seek the MLE solution, check the AIC values, and test the KS statistic by the Kolmogorov-Smirnov function. Then by simulation runs, estimate the error ranges of the obtained parameters, and the P-value of the observed KSr statistic.
- Method 2: Minimize KSr to obtain the solution, check the AIC values, and test the KS statistic by the Kolmogorov-Smirnov function. Then by simulation runs, estimate the error ranges of the obtained parameters, and the P-value of the observed KSr statistic.

Method 2 was not applied to the power-law model because the deviations of the model at the tail are large and the introduction of KSr may not make sense.

## 4. FITTING RESULTS

### 4.1. Power Law

Figure 4 shows the results of power-law fitting. The MLE solution for the exponent is  $\alpha_1 = 2.91$ , and the KS statistic is large,  $\sqrt{N_s} \text{KS} = 4.1$ . Therefore, the probability of obtaining such a value or larger is infinitesimally small, and the model is safely rejected.

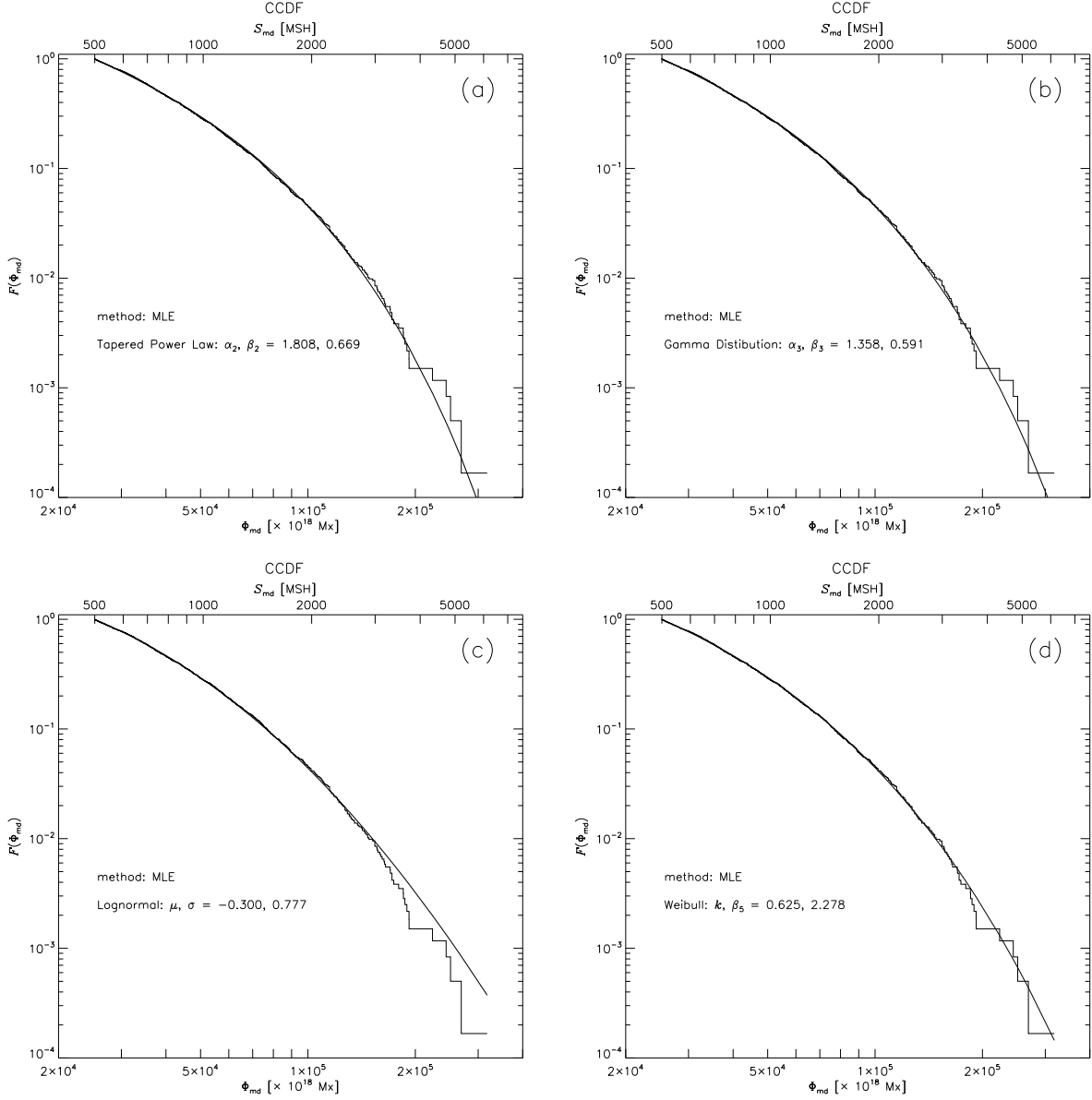


**Figure 5.** MLE fits to the complimentary cumulative distribution functions  $F(\Phi)$  using models of (a) tapered power law, (b) gamma, (c) lognormal, and (d) Weibull distributions.

#### 4.2. Two-Parameter Models

Figures 5 (a)–(d) show the results of fitting by adopting MLE solutions (Method 1). Method 2 also gives similar plots. In Figure 6, both the CCDF and emergence rates  $f(\Phi_{\text{md}})$  together with the fitted functions are given by applying Method 2 to the gamma distribution model, which is our most favorable model.

Table 2 summarizes, for MLE and KSr=min (except for power law) methods respectively, the obtained parameter values (with error ranges), relative AIC values, KS statistics and its theoretical probability, and P-values based on the KSr statistic. Here  $\Delta\text{AIC}$  ( $\Delta\text{BIC} = \Delta\text{AIC}$  among the two-parameter models) means the values of AIC with respect to its smallest value in the models (which

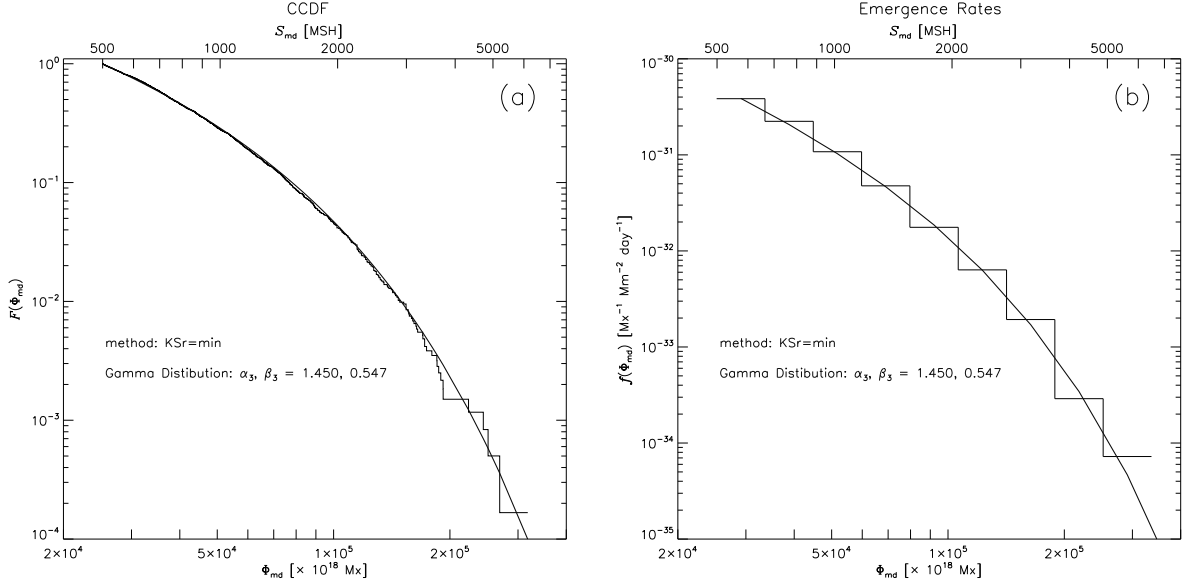


**Figure 6.** (a) A fit to the complimentary cumulative distribution function (CCDF)  $F(\Phi_{\text{md}})$  using the gamma distribution model and by minimizing the KSr metric. (b) The gamma-distribution fit of panel (a) for  $F(\Phi_{\text{md}})$  is converted to the probability distribution function  $f(\Phi_{\text{md}})$  and overplotted on the histogram of the data.

happened to take place for the MLE model applied to the Weibull distribution). Strictly speaking, AIC is defined when LLH is maximized [the MLE solution, Equation (5)], but we also applied the same formula by replacing  $\max(\text{LLH})$  with LLH from a particular solution not maximizing LLH. Therefore, for each model,  $\Delta\text{AIC}$  is smaller for the MLE solution than for the solution with  $\text{KSr}=\min$ . Likewise, the P-value based on KSr is larger (better fitting) for the solution with  $\text{KSr}=\min$  compared to the MLE solution.

The following properties can be found on this table.

1. The AIC values of the two-parameter models are much smaller than the case of the power law, so that all these four models are better than the power law. The four models show  $\Delta\text{AIC}$  values less than 5 and cannot be discriminated.
2. From the KS probabilities, the MLE solutions show better performance but the  $\text{KSr}=\min$  solutions are also acceptable.
3. From the P-values of the KSr metric, the solutions minimizing KSr show better performance but the MLE solutions are also acceptable.
4. The power-law indices of the tapered power law and the gamma distributions are  $\alpha_2 = 1.8\text{--}1.9$  and  $\alpha_3 = 1.35\text{--}1.45$ . The reason why  $\alpha_2 > \alpha_3$  is given in Appendix A.4; the tapered power-law distribution actually contains a mixture of two exponents  $\alpha_2$  and  $\alpha_2 - 1$ , and its overall behavior is somewhere between them. If we extend the PDF toward smaller  $\Phi_{\text{md}}$  values, the tapered power-law distribution asymptotically approaches the power law with exponent  $\alpha_2$ . In any case it is important to point out that both distributions show the power-law-like behavior

with exponent less than 2, namely the overall contributions to the magnetic flux supply come mostly from large  $\Phi_{\text{md}}$  regions.

5. As we discuss later (Figure 7), the behavior of lognormal and Weibull distributions extended to smaller values of  $\Phi_{\text{md}}$  is different from the tapered power-law and gamma distributions (the latter two behave essentially like a power law with exponent  $\simeq 1.35$ – $1.9$ ). The Weibull distributions approach toward a very flat power-law distribution  $\propto \Phi_{\text{md}}^{-0.4}$ , and the lognormal distributions decrease toward small  $\Phi_{\text{md}}$ . Therefore, our preferred models are the tapered power-law and gamma distributions.
6. The tapered power-law and gamma distributions show a steep fall-off for large  $\Phi_{\text{md}}$  values, steeper than power laws, indicating that the probability of having extremely large active regions is vanishingly small and there is a practical upper limit in the size and magnetic flux of emerging active regions.

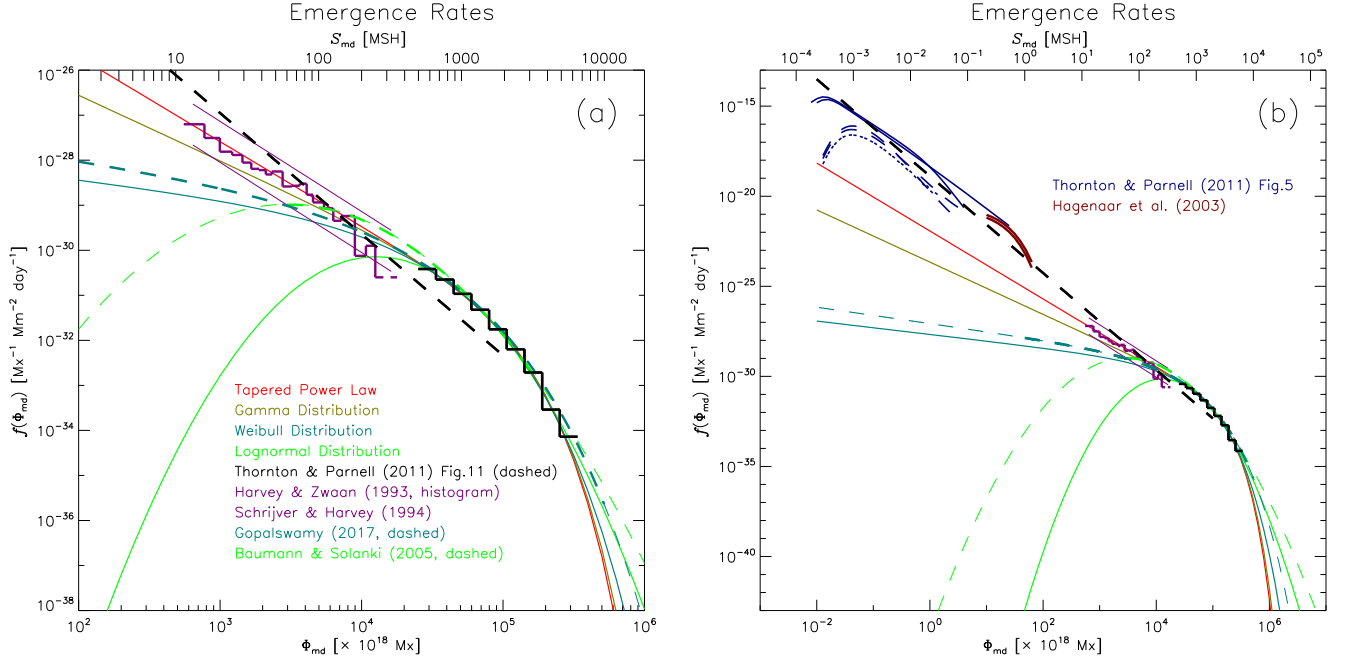


**Figure 7.** (a) Comparison of magnetic flux emergence rates  $f(\Phi_{\text{md}})$ . The histogram drawn with a thick black line is our data. Four kinds of fits by minimizing the KSr metric are shown, respectively, for tapered power-law (red), gamma (olive), Weibull (teal green), and lognormal (lime green) distributions. The black dashed line of power-law exponent 2.69 is from Thornton & Parnell (2011). The histogram shown in purple is from Harvey & Zwaan (1993), and the two parallel lines in purple are the power laws of exponent=2 (Schrijver & Harvey 1994) representing their amplitude ranges in solar activity minima/maxima. The dashed curve in lime green is the lognormal fit from Baumann & Solanki (2005). The dashed curve in teal green is the Weibull function fit from Gopalswamy (2018). (b) Same as panel (a) but the plotting range is extended to smaller flux values. Newly added graphs are the SOHO/MDI data from Hagenaar et al. (2003, maroon) and the Hinode/SOT data from Thornton & Parnell (2011, navy blue).



## 5. COMPARISON WITH PUBLISHED RESULTS

In this section, we will compare our results on the two-parameter models with the published observational data and fitting results. In Figure 7a which shows the flux emergence rates  $f(\Phi_{\text{md}})$ , the histogram in a thick black line is our data ( $500 \text{ MSH} \leq S_{\text{md}} \leq 6132 \text{ MSH}$ ,  $2.53 \times 10^{22} \text{ Mx} \leq \Phi_{\text{md}} \leq 3.18 \times 10^{23} \text{ Mx}$ ). Four solid curves show our fits by minimizing the KSr metric; tapered power-law (red), gamma (olive), Weibull (teal green), and lognormal (lime green) distributions. They are extended down to  $\Phi_{\text{md}} = 10^{20} \text{ Mx}$  ( $S_{\text{md}} \simeq 2 \text{ MSH}$ ) and up to  $\Phi_{\text{md}} = 10^{24} \text{ Mx}$  ( $S_{\text{md}} \simeq 19000 \text{ MSH}$ ). Toward the smaller ends of  $\Phi_{\text{md}}$ , the tapered power-law, gamma, and Weibull distributions approach power laws with exponents 1.89, 1.45, and 0.37, respectively.

The histogram in a thick purple line is taken from [Harvey & Zwaan \(1993\)](#), who derived the emergence rates of bipolar active regions using the data obtained at NSO Kitt Peak ([Livingston et al. 1976](#)). [Schrijver & Harvey \(1994\)](#) reported that this distribution is fitted by a power law with exponent 2, and the amplitudes vary by roughly a factor of 10 between activity minimum and maximum, as shown by two parallel lines in purple.

The thick dashed curve in lime green reproduces the lognormal fit to the RGO data ( $S_{\text{md}} \geq 60 \text{ MSH}$ ) by [Baumann & Solanki \(2005\)](#), extended down to  $S_{\text{md}} \simeq 2 \text{ MSH}$  (thin dashed curve). Below the peak at  $S_{\text{md}} \simeq 62.2$ , the curve goes down to  $f \rightarrow 0$ . Our lognormal fit peaks at  $S_{\text{md}} \simeq 250 \text{ MSH}$  and then decreases to  $f \rightarrow 0$ . At least for our lognormal fitting, this decrease is not due to small fluxtubes losing their darkness, because even the smallest regions (500 MSH) in our sample are fairly large regions. Rather, this is a result of the shape of the observed distribution that bends down toward large  $\Phi_{\text{md}}$ , and the derived  $\mu$  value may not represent any physical significance. [Bogdan et al. \(1988\)](#) gave the values 0.34–0.62 MSH for the peak of the instantaneous distribution function of sunspot umbral areas modeled by lognormal distribution.

The thick dashed curve in teal green reproduces the Weibull fit to the RGO and USAF/NOAA data by [Gopalswamy \(2018\)](#), which covered all the data  $S_{\text{md}} \geq 1 \text{ MSH}$ . The curve is very close to our Weibull fit.

In Figure 7b, we extended the plot range to  $10^{15} \text{ Mx} \leq \Phi_{\text{md}} \leq 10^{25} \text{ Mx}$  ( $2.3 \times 10^{-5} \text{ MSH} \lesssim S_{\text{md}} \lesssim 1.9 \times 10^5 \text{ MSH}$ ), and added two more data sets. The thick solid curve in brown is from [Hagenaar et al. \(2003\)](#), who investigated the emergence rates of small-scale bipolar magnetic patches (ephemeral regions) using the data from SOHO/MDI. The thick curves in navy blue (solid, dashed, dotted) are from [Thornton & Parnell \(2011, Figure 5\)](#), who analyzed the emergence rates of small-scale magnetic patches using the data from Hinode/SOT. The thin dashed line in teal green is the downward extension of [Gopalswamy \(2018\)](#)'s Weibull distribution.

The thick dashed lines in black in Figures 7a and 7b show the power law of exponent 2.69 suggested by [Thornton & Parnell \(2011\)](#) to cover all the way from small-scale flux concentrations to large active regions. Our picture is different from theirs; the flux emergence rates of active regions are characterized by a power-law-like behavior of exponents between 1.45 (olive) and 1.89 (red) in Figure 7. Our results are roughly consistent with the observations by [Harvey & Zwaan \(1993\)](#), who also showed that the distribution amplitudes varied by a factor of 10 between activity minima and maxima. Ephemeral regions and much smaller flux concentrations may have a power-law distribution with exponent 2.69, but they show little changes (or even anti-phase changes; [Hagenaar et al. 2003](#)) with the solar cycle, and they may give way to the active region component somewhere at around  $\Phi_{\text{md}} \simeq 10^{20} \text{ Mx}$ . The exponent larger than 2 in small-scale flux concentrations means dominant contributions

of flux emergence in the smallest end of the distribution function. Those small-scale flux emergence may be sustained by a local dynamo (Cattaneo 1999; Buehler et al. 2013). The total (unsigned) magnetic flux on the Sun in scales exceeding a few arcseconds ( $\gtrsim 1000$  km) varies in phase with the solar cycle (Arge et al. 2002), and the flux at activity maximum is about four times the flux at minimum. Therefore, flux emergence in small scales would not accumulate to systematically overwhelm the magnetic flux from active regions.

**Table 3.** Sunspot area, magnetic flux, and interval of appearance

$S$ [MSH]	$\Phi$ [Mx]	Interval [year]	$S$ [MSH]	$\Phi$ [Mx]	Interval [year]
500	$2.5 \times 10^{22}$	$5.242 \pm 0.001 \times 10^{-2}$	$6.2^{+0.5}_{-0.4} \times 10^3$	$(3.2^{+0.2}_{-0.2}) \times 10^{23}$	$1.0 \times 10^3$
1000	$5.1 \times 10^{22}$	$1.82 \pm 0.04 \times 10^{-1}$	$7.9^{+0.7}_{-0.5} \times 10^3$	$(4.1^{+0.4}_{-0.3}) \times 10^{23}$	$1.0 \times 10^4$
2000	$1.0 \times 10^{23}$	$1.20 \pm 0.04 \times 10^0$	$9.7^{+1.0}_{-0.7} \times 10^3$	$(5.0^{+0.5}_{-0.4}) \times 10^{23}$	$1.0 \times 10^5$
3000	$1.5 \times 10^{23}$	$6.0^{+0.9}_{-0.8} \times 10^0$	$1.15^{+0.12}_{-0.09} \times 10^4$	$(6.0^{+0.6}_{-0.5}) \times 10^{23}$	$1.0 \times 10^6$
6132	$3.2 \times 10^{23}$	$5.2^{+3.7}_{-2.2} \times 10^2$	$1.51^{+0.18}_{-0.14} \times 10^4$	$(7.9^{+1.0}_{-0.7}) \times 10^{23}$	$1.0 \times 10^8$
10000	$5.2 \times 10^{23}$	$8.2^{+17}_{-5.5} \times 10^4$	$1.83^{+0.23}_{-0.17} \times 10^4$	$(9.6^{+1.2}_{-0.9}) \times 10^{23}$	$4.6 \times 10^9$

The ranges of values are based on the 1- $\sigma$  error ranges given in Table 2, namely  $\alpha_3 = 1.450 \pm 0.224$ ,  $\beta_3 = 0.547 \pm 0.083$ .

### 5.1. Emergence Frequency of Large Sunspots

Based on the fitting results, we are able to predict the expected frequencies of large sunspots. Table 3 shows, by using the model of gamma distribution with parameter values determined from KSr=min ( $\alpha_3 = 1.450 \pm 0.224$ ,  $\beta_3 = 0.547 \pm 0.083$ ), the expected appearance intervals as a function of sunspot area (left half of the table), and the expected sunspot areas for the specified values of appearance intervals (right half of the table). The ranges of values given are based on the 1- $\sigma$  error ranges given in Table 2. It turned out that the errors in  $\alpha_3$  and  $\beta_3$  are roughly inversely correlated, so that the ranges of values shown in Table 3 correspond to  $(\alpha_3, \beta_3) = (1.450 + 0.224, 0.547 - 0.083)$  and  $(1.450 - 0.224, 0.547 + 0.083)$ .

The time interval for regions with flux larger than  $\Phi$  to appear is given by  $[F(\Phi)N_s/T]^{-1}$  ( $N_s = 2995$ ,  $T = 146.7$  years). The sunspots larger than 500 MSH are expected to appear at a rate of every 19 days. The regions as large as or exceeding the largest region in our database (6132 MSH) are expected to appear every 520 years. Beyond roughly 10000 MSH, the interval becomes longer than  $8 \times 10^4$  years, and even after the lifetime of the Solar System ( $4.6 \times 10^9$  years), one can only expect a region as large as  $1.8 \times 10^4$  MSH. These are due to the exponential decline of the probability distribution function. By taking into account the 1- $\sigma$  errors, the expected interval for 10000 MSH regions is reduced to  $2.7 \times 10^4$  years, and  $2.1 \times 10^4$  MSH is the possible maximum size after  $4.6 \times 10^9$  years.

## 6. FORWARD MODELING

In the analysis so far, we have assumed that the maximum sunspot areas observed on the visible hemisphere are the true maximum areas, which might take place on the back side of the Sun, though.

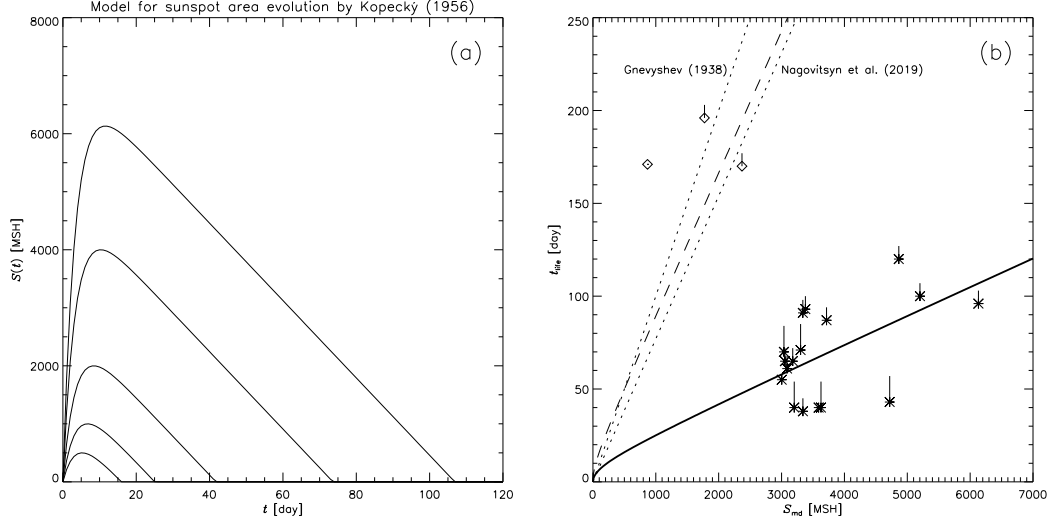


**Figure 8.** A model for sunspot area evolution proposed by [Kopecký \(1956\)](#). (a) The area  $S(t)$  as a function of time  $t$  in day is given for a set of parameters  $(a, b) = (0.3, 20.0)$ , by changing  $K$ . The curves correspond, from the lowest to the highest, to the maximum-development areas  $S_{\text{md}}$  of 500, 1000, 2000, 4000, and 6132 MSH. (b) The lifetime  $t_{\text{life}}$  as a function of maximum-development area  $S_{\text{md}}$ . The thick solid line is our adopted model with  $(a, b) = (0.3, 20.0)$ , while the dashed line represents the original relation of [Kopecký \(1956\)](#) with  $(a, b) = (0.3, 4.0)$ . The dotted lines are the formulae given by [Gnevyshev \(1938\)](#) and [Nagovitsyn et al. \(2019\)](#), respectively. The diamond signs and asterisks denote the lifetimes of regions taken from published data ([Kopecký 1984](#); [Spencer Jones 1955](#)).

The errors caused by this assumption cannot be corrected, but we may be able to estimate the effects by a forward modeling, namely, by assuming a typical time evolution of sunspot areas we can simulate such effects. As a biproduct, we can convert our maximum-development distribution functions to instantaneous distribution functions.

### 6.1. Model

Many models have been proposed to represent the time evolution of sunspot areas (e.g. [Kopecký 1956](#); [Antalova & Macura 1986](#); [Howard 1992](#); [Hathaway & Choudhary 2008](#)). Here we use the model proposed by [Kopecký \(1956\)](#) because of its analytical simplicity and versatility. The time evolution of sunspot area  $S(t)$  is described by a differential equation

$$\frac{dS}{dt} = -aS + K - bt \quad (t \geq 0), \quad (6)$$

where  $a$ ,  $b$ , and  $K$  are parameters;  $(a, b)$  control the shape of the time profile, and  $K$  controls the maximum size of the region. The solution to this equation is given as

$$S = \frac{1}{a} \left[ \left( K + \frac{b}{a} \right) (1 - e^{-at}) - bt \right], \quad (7)$$

and  $S(t)$  takes the maximum value

$$S_{\text{md}} = \frac{K}{a} - \frac{b}{a^2} \ln \frac{aK + b}{b} \quad (8)$$

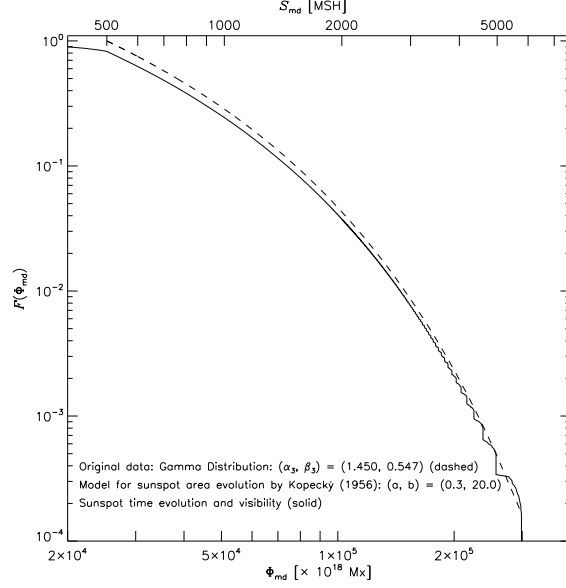


**Figure 9.** Effects of time evolution of sunspot areas were estimated by using a model by [Kopecký \(1956\)](#). The dashed curve is the model generated from a gamma distribution with  $\alpha_3 = 1.450$  and  $\beta_3 = 0.547$  which reproduces the data well. The solid curve shows the distribution expected from the model by taking into account the visibility probability of regions.

at time

$$t_{\text{md}} = \frac{1}{a} \ln \frac{aK + b}{b}. \quad (9)$$

$S(t)$  starts from  $S(0) = 0$  and comes back to  $S(t_{\text{life}}) = 0$  where

$$\frac{1 - \exp(-at_{\text{life}})}{at_{\text{life}}} = \frac{b}{aK + b}. \quad (10)$$

The solution for  $t_{\text{life}}$ , if  $at_{\text{life}} \gg 1$ , is

$$t_{\text{life}} \simeq \frac{K}{b} + \frac{1}{a}, \quad (11)$$

and if  $at_{\text{life}} \ll 1$ , it is

$$t_{\text{life}} \simeq \frac{2K}{aK + b}. \quad (12)$$

[Kopecký \(1956\)](#) used the empirical relations  $t_{\text{life}}[\text{days}] \simeq 0.1S_{\text{md}}[\text{MSH}]$  ([Gnevyshev 1938](#)) and  $t_{\text{life}}/t_{\text{md}} \simeq 0.094S_{\text{md}}[\text{MSH}] + 9.3$  ([Kopecký 1953](#)) and adopted  $(a, b) = (0.3, 4.0)$  which roughly reproduces these empirical relations for  $S_{\text{md}} \lesssim 400$  MSH. However, this setting makes the lifetimes of 500 MSH (minimum in our database) and 6132 MSH (maximum) regions as 50 days (1.8 solar rotations) and 480 days (1.3 years, 17.6 solar rotations) respectively, which look too long. [Nagovitsyn et al. \(2019\)](#) suggested  $t_{\text{life}}[\text{days}] \simeq 0.077S_{\text{md}}[\text{MSH}]$ , a slightly shorter lifetime for the specified  $S_{\text{md}}$  compared to [Gnevyshev \(1938\)](#), but this also gives large values of lifetimes. According to [Kopecký \(1984\)](#) the longest lifetime of regions in the RGO observations was 8 solar rotations (RGO recurrent series No. 2094, 1970 June 11 – December 23, 195 days, maximum area = 1774 MSH). The region of largest

area (RGO region 14886, 6132 MSH) had a lifetime of 95 days (1947 February 5 – May 11, observed for 4 rotations).

As will be discussed in Section 6.3, the gamma function model for  $F(\Phi_{\text{md}})$  described in Section 5.1 gives the instantaneous distributions of sunspot area or magnetic flux which are consistent with the observed distributions only if the region lifetimes are much shorter; a reasonable value we found is  $(a, b) = (0.3, 20.0)$ . The value of  $a$  is fixed to 0.3, because the rise time of region growth ( $\simeq 1/a$ ) does not strongly depend on the region size. The lifetimes of the 500 and 6132 MSH regions in this model are 16 and 107 days, respectively. Figure 8a shows the time profiles  $S(t)$  derived for  $(a, b) = (0.3, 20.0)$  and for several values of  $S_{\text{md}}$ . Figure 8b compares the models with  $(a, b) = (0.3, 4.0)$  and  $(0.3, 20.0)$ , and other published results of sunspot lifetimes. The diamond signs denote the data points of three longest-lived regions listed in Kopecký (1984). The asterisks denote the lifetimes of maximum sunspot areas  $> 3000$  MSH taken from Spencer Jones (1955). The regions whose emergence or decay (either of them) were not observed on the visible disk have uncertainties in their lifetimes between 1 and 13 days. Hence we roughly assigned a 7-day error bar. The regions whose emergence and decay (both of them) were not observed on the visible disk were assigned with a 14-day error bar. The model with  $(a, b) = (0.3, 20.0)$  goes through the middle of the data points representing large ( $> 3000$  MSH) regions.

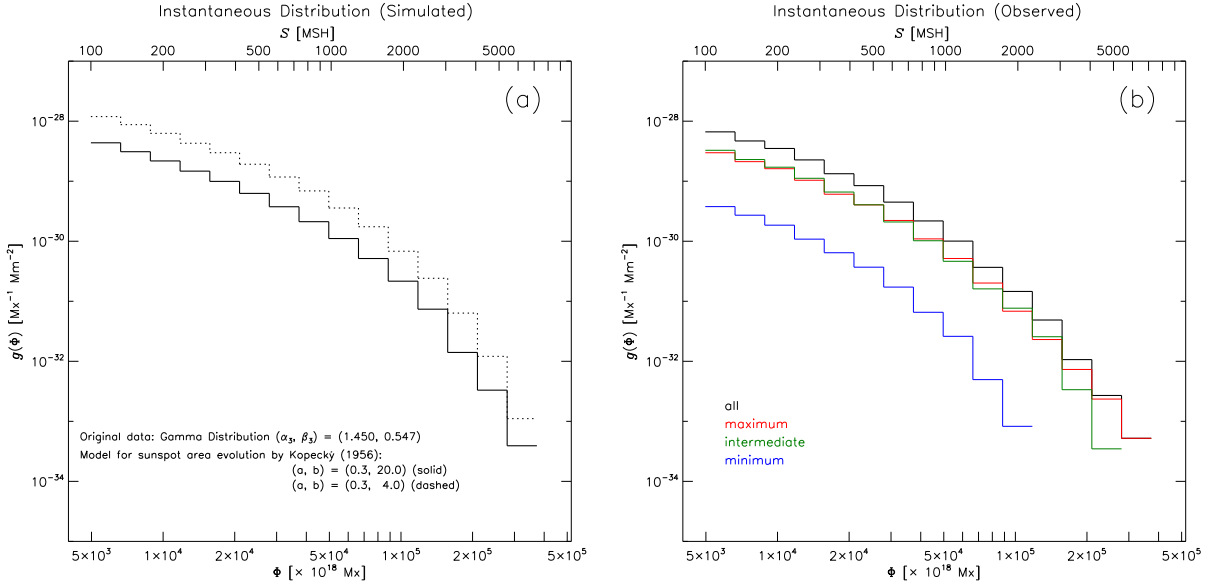


**Figure 10.** (a) The histogram of the probability distribution function  $g(\Phi)$  of instantaneous distribution of magnetic flux, derived from a gamma distribution with  $\alpha_3 = 1.450$  and  $\beta_3 = 0.547$  combined with the sunspot area evolution models of Figure 8. The solid and dashed histograms correspond to  $(a, b) = (0.3, 20.0)$  and  $(a, b) = (0.3, 4.0)$ , respectively. (b) The corresponding distributions derived from observations of RGO and NOAA. The histogram in black was derived by using all the data with areas larger than 100 MSH, while red, green, and blue ones are based on data from maximum, intermediate, and minimum phases of activity defined in Table 4.

## 6.2. Effects of Time Evolution

The effects of time evolution of sunspots were simulated as follows. By adopting a model of gamma distribution with  $\alpha_3 = 1.450$  and  $\beta_3 = 0.547$ , we have generated  $N_s$  samples ( $N_s = 2995$ ) of  $\Phi_{\text{md}}$  by

$$F(\Phi_i) = \frac{i - 0.5}{N_s} \quad (i = 1, 2, \dots, N_s). \quad (13)$$

Then each model was placed at 27 equal-distant longitudes (27 is a rough number of solar rotation period in days), magnetic flux was converted to sunspot area by Equation (1), and was evolved according to Equation (7). The observed maximum values of  $S(t)$  in the longitude ranges of  $\pm 80^\circ$  were recorded, converted to magnetic flux, and the CCDF was generated.

The solid curve in Figure 9 shows the result, compared with the true distribution designated by the dashed curve. After fitting the model, we found  $\alpha_3 = 1.319$  and  $\beta_3 = 0.590$ . The flattening of the distribution from  $\alpha_3 = 1.450$  to  $\alpha_3 = 1.319$  (by about 0.13) is because we underestimated  $S_{\text{md}}$ , and the data points on the original model (dashed) were shifted toward left on the graph. From this we may estimate that  $\alpha_3 = 1.450$  derived from observations would actually be around  $\alpha_3 = 1.68$ , but still our conclusion will hold that the power-law exponent is less than 2.

**Table 4.** Summary of observed quantities

Data source	Time span [year]	Regions per	Daily region counts	Number of	Observed maximum values			
		full Sun <sup>a</sup>	per hemisphere	observations	Total	Total	Region	Region
		$N_s$	$N_{\text{rd}}$	$N_d$	area	flux	lifetime	counts
		( $S_{\text{md}} \geq$ 500 MSH)	( $S \geq$ 500 MSH)	( $S_{\text{hs}} \geq$ 10 MSH)	[MSH]	[Mx]	[d]	
All	146.71	2995	$1.97 \times 10^4$	$4.42 \times 10^4$	8382 <sup>b</sup>	$4.36 \times 10^{23}$	195 <sup>c</sup>	26 <sup>d</sup>
Maximum	35.26	1466	$0.99 \times 10^4$	$1.28 \times 10^4$	8382	$4.36 \times 10^{23}$		
Minimum	37.65	114	$0.06 \times 10^4$	$0.71 \times 10^4$	2268	$1.16 \times 10^{23}$		
Intermediate	73.80	1415	$0.92 \times 10^4$	$2.43 \times 10^4$	8080	$3.54 \times 10^{23}$		

<sup>a</sup> Recurrent regions were manually picked up and counted only once when they showed the largest area.

<sup>b</sup> 1947 April 8

<sup>c</sup> RGO recurrent series No. 2094, 1970 June 11 – December 23 (Kopecký 1984).

<sup>d</sup> 1937 July 12

### 6.3. Instantaneous Distribution

Once we have a model of time evolution of sunspot areas, we can generate the instantaneous distribution function from the distribution of maximum-development areas. First consider a simple case where the time evolution is represented by a step function (i.e. a spot appears with a maximum-development area and stays so until it suddenly disappears). If the lifetimes of regions do not depend on the areas and take a fixed value, the instantaneous distribution function is the same as the maximum-development distribution function. If the lifetimes are proportional to the areas, the instantaneous distribution function would be flatter than the maximum-development distribution function because larger regions live longer and have higher probability of existence in snapshot data.



**Table 5.** Simulation runs for Sun-as-a-star parameters.

Data source	Simulation parameters	Regions per full Sun <sup>a</sup> $N_s$ ( $S_{\text{md}} \geq$ 10 MSH)	Simulated maximum values			
			Total	Total	Region	Region
			area <sup>b</sup>	flux	lifetime	counts
			[MSH]	[Mx]	[d]	
All	(0.3, 20.0)	$8.5 \times 10^4$	8270	$4.30 \times 10^{23}$	101	15
Maximum	(0.3, 20.0)	$4.2 \times 10^4$	7420	$3.85 \times 10^{23}$	93	22
Minimum	(0.3, 20.0)	$0.3 \times 10^4$	3680	$1.90 \times 10^{23}$	65	5
Intermediate	(0.3, 20.0)	$4.0 \times 10^4$	6120	$3.17 \times 10^{23}$	93	14
Combined	(0.3, 20.0)	$8.5 \times 10^4$	7420	$3.85 \times 10^{23}$	93	22
Maximum <sup>c</sup>	(0.3, 4.0)	$4.2 \times 10^4$	13770	$7.19 \times 10^{23}$	413	44

<sup>a</sup> The number of samples in the gamma function model with minimum values extended down to  $4.86 \times 10^{20}$  Mx (10 MSH).

<sup>b</sup> The numbers do not have significance of four or more digits because of the nature of the simulation. They are arbitrarily rounded off to the nearest ten.

<sup>c</sup> This is an artificial case of region lifetimes longer than the standard case of  $(a, b) = (0.3, 20.0)$ .

In the general cases where the time evolution of sunspot areas is a function of time like in Equation (7), one must resort to numerical simulations to estimate the instantaneous distribution function of sunspot areas or flux emergence rates.

By adopting a model of gamma distribution with  $\alpha_3 = 1.450$  and  $\beta_3 = 0.547$ , we have generated  $N_s$  samples of  $\Phi_{\text{md}}$  by Equation (13) and converted them to  $S_{\text{md}}$  by Equation (1). This time we have extended the lower limit of sunspot area and flux to 100 MSH and  $4.97 \times 10^{21}$  Mx, so that  $N_s = 1.8 \times 10^4$ ; the number of regions with  $S_{\text{md}} \geq 500$  MSH was still 2995. Next we used Equation (7) to evaluate and record daily values of  $S(t)$  and  $\Phi(t)$ , leading to data samples  $N_{\text{rd}} = 1.90 \times 10^4$  [region  $\times$  day per hemisphere] for  $S(t) \geq 500$  MSH. In this process we introduced a filter made of 13 consecutive 1's followed by 14 consecutive 0's, mimicking a 27-day modulation of visibility. This filter, replicated many times to cover the lifetimes of regions and its initial point randomly shifted between 0 and 26-th points, was multiplied to daily values of  $S(t)$  and  $\Phi(t)$ . Thus we derived the histogram per unit area (Figure 10a, solid histogram) by taking  $A$ =area of the solar hemisphere= $3.1 \times 10^6$  Mm<sup>2</sup>. Roughly this distribution is fitted by a gamma distribution with  $\alpha_3 = 0.928$  and  $\beta_3 = 0.654$ . The power-law exponent decreased ( $1.450 \rightarrow 0.928$ ), giving a much flatter distribution. The observed value of  $N_{\text{rd}}$  obtained by counting regions with  $S(t) \geq 500$  MSH every day is  $1.97 \times 10^4$  [region  $\times$  day per hemisphere] and roughly agrees with the simulated results. On the other hand if we used the evolution parameters  $(a, b) = (0.3, 4.0)$ , we ended up with a much larger value  $N_{\text{rd}} = 6.10 \times 10^4$  [region  $\times$  day per hemisphere], and the resulting histogram is shown as the dashed line in Figure 10a. As a matter of fact we have selected the values  $(a, b) = (0.3, 20.0)$  so that the value of  $N_{\text{rd}}$  roughly matches the observation.

In deriving the instantaneous distribution functions of sunspot magnetic flux from observed data, we have divided the data into three periods; activity maximum, intermediate state, and activity minimum. (The reason why we did so is given in Section 6.4.) The dates (year and month) of activity maxima/minima are taken from SILSO (Sunspot Index and Long-term Solar Observations)<sup>10</sup>, and we will define the maximum/minimum periods as within 1.356 years from the maximum/minimum dates. The mean lengths of the maximum, intermediate (between maximum and minimum periods), and minimum states are 2.712, 5.424, and 2.712 years, respectively. The mean length of 13 cycles studied here is 10.85 years, and  $10.85/8 = 1.356$  years. The regions of  $N_s = 2995$  with  $S_{\text{md}} \geq 500$  MSH were divided into maximum (1466), minimum (114), and intermediate (1415) states, respectively (Table 4).

Figure 10b shows the observed instantaneous distribution functions of sunspot magnetic flux when all the data were used (black histogram) as well as the three activity phases were treated separately (red, green, and blue histograms). We have used all the data with  $S \geq 100$  MSH. The histograms are all similar, meaning that they only change the magnitude and not the form of distribution. Particularly the histogram using all the data is reproduced well by the simulated results with  $(a, b) = (0.3, 20.0)$  (Figure 10a, solid histogram).

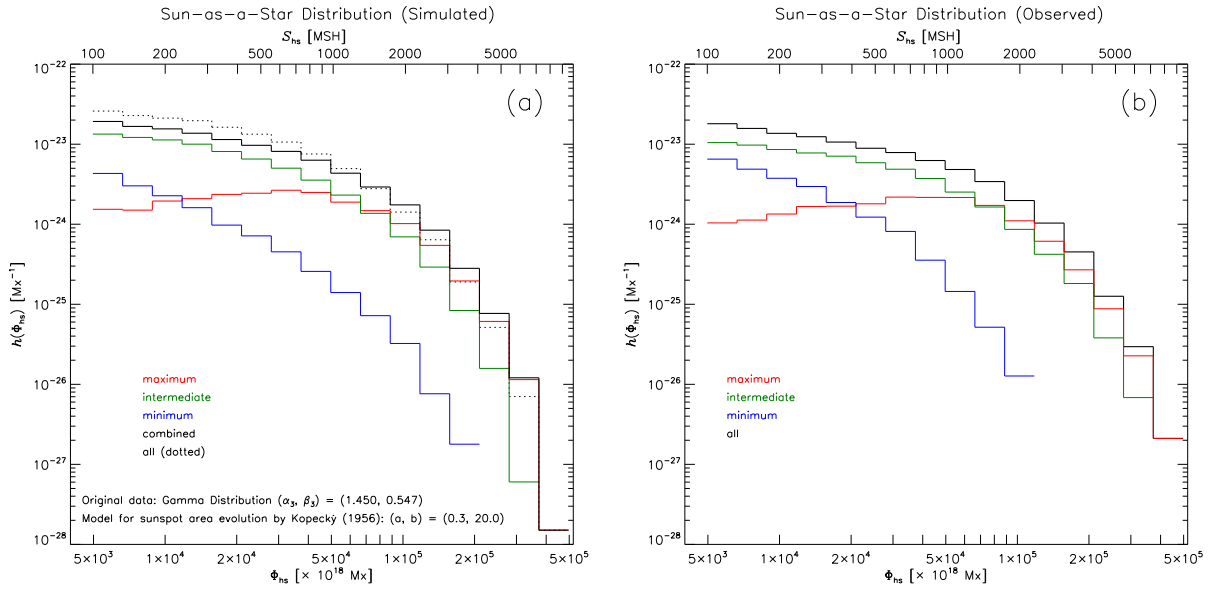


**Figure 11.** (a) The histograms of the probability distribution function  $h(\Phi_{\text{hs}})$  of magnetic flux summed over the hemisphere, derived from a gamma distribution with  $\alpha_3 = 1.450$  and  $\beta_3 = 0.547$  combined with the sunspot area evolution model of Figure 8. The dotted histogram in black was derived by simply using all the generated data. The histograms in red, green, and blue were derived by mimicking activity maximum, intermediate, and minimum states as defined in Table 4. The solid histogram in black was made by combining these three histograms. (b) The corresponding distributions derived from observations of RGO and NOAA. The histogram in black was derived by using all the data with areas larger than 10 MSH, while red, green, and blue ones are based on data from activity maximum, intermediate, and minimum phases of activity defined in Table 4.

<sup>10</sup> <https://wwwbis.sidc.be/silso/cyclesminmax>

#### 6.4. *Sun-as-a-Star Distributions*

From the instantaneous distribution of magnetic flux or sunspot areas, we can also derive the distribution function of total magnetic flux or total area of sunspot regions, summed over the hemisphere. This is a more fundamental quantity in considering solar irradiance modulation or luminosity variations of stars by starspots.

By adopting a model of gamma distribution with  $\alpha_3 = 1.450$  and  $\beta_3 = 0.547$ , we have generated  $N_s = 2995$  samples of  $\Phi_{\text{md}}$  by Equation (13) and converted them to  $S_{\text{md}}$  by Equation (1). The distribution was extended down to  $S_{\text{md}} = 10$  MSH, because in the process of time evolution, regions with  $S < 500$  MSH were generated, and these regions also contributed to the total area of sunspots. Then the models were distributed randomly over the time period of  $0 \leq t \leq t_0 = 146.7$  years, and were evolved according to Equation (7). If the time evolution of a region hit the end of the time domain  $t = t_0$ , the profile was folded and continued to  $t = 0$ , to make the statistical distribution stationary in time. The filter of 13 consecutive 1's and 14 consecutive 0's was multiplied to  $S(t)$  as in Section 6.3. The daily summed values of magnetic flux over the solar hemisphere,  $\Phi_{\text{hs}}$ , were recorded, and the histogram of PDF was generated (Figure 11a). In Figure 11, in addition to the abscissa in terms of  $\Phi_{\text{hs}}$ , the scale is also given for the sunspot areas summed over the hemisphere,  $S_{\text{hs}}$ .

Figure 11a shows four histograms thus generated. The dotted histogram is the one that was made by simply using all the generated data values. The result is rather counter-intuitive in that the distribution is very flat at the lower end; actually it has a peak at 120 MSH. By looking at the histograms derived from observations (Figure 11b), the histogram using all the data is monotonically decreasing, and those derived from activity maximum, intermediate, and minimum states show different behavior. In particular the histogram of the activity maximum period shows a peak at around  $3 \times 10^{22}$  Mx (650 MSH), but the sum of the three histograms (red, green, and blue) gives the histogram in black which is monotonically decreasing.

The red, green, and blue histograms in Figure 11a obtained from simulations mimic the activity maximum, intermediate, and minimum states. If all combined, we obtain the histogram in a black solid line which roughly reproduces the observed histogram in Figure 11b (black). Here it must be stressed that the sum of the red, green, and blue histograms in Figure 11a does not lead to the black dotted histogram (derived from using all the data) but to the black solid histogram. In the simulated data the solar cycle modulation was not built in and had to be introduced manually. The black dotted histogram (derived from using all simulated data) is similar in shape to the one derived from the intermediate activity state, meaning that the entire simulated data without cycle modulation represent an intermediate activity lasting the entire data period of 146.7 years.

The corresponding histograms (red, green, and blue) in Figures 11a and b do not match so well, in various reasons. Our model for the time evolution of sunspot areas is a very idealized one. The lifetime of a region was assumed to be a unique function of maximum-development area, but in reality there should be a statistical distribution of region lifetimes for a given maximum-development area. The division of data into three phases (activity maximum, intermediate, and minimum states) was made by a very simple procedure. Nevertheless the maximum hemispheric summed area of sunspots expected from simulations is about 7420 MSH, which is not very far from the observed maximum value, 8382 MSH.

Figure 12 compares two cases of maximum activity phase; one is the same as in Figure 11 (except for the normalization parameter  $T$ ; Appendix A.2) and the other adopts the parameter setting

$(a, b) = (0.3, 4.0)$ , i.e. the value originally suggested by [Kopecký \(1956\)](#) to reproduce the empirical relations  $t_{\text{life}}[\text{days}] \simeq 0.1 S_{\text{md}}[\text{MSH}]$  by [Gnevyshev \(1938\)](#). The two histograms are not monotonic and have peaks at  $\Phi_{\text{hs}} = 3.4 \times 10^{22} \text{ Mx}$  ( $S_{\text{hs}} = 680 \text{ MSH}$ ) for the former case and at  $\Phi_{\text{hs}} = 1.8 \times 10^{23} \text{ Mx}$  ( $S_{\text{hs}} = 3500 \text{ MSH}$ ) for the latter case. The maximum value of the hemispheric summed area for the latter case is 13770 MSH.

The summed area of sunspots can be converted to the modulation in total solar irradiance (TSI,  $\simeq 1361 \text{ W m}^{-2}$ ; [Kopp 2021](#)) by

$$\frac{\Delta \text{TSI}}{\text{TSI}} = c \frac{S_{\text{h}}[\text{MSH}]}{2 \times 10^6} \quad (14)$$

with  $c \simeq 0.22\text{--}0.31$  ([Hudson et al. 1982](#)). If we take the observed maximum value of  $S_{\text{hs}} = 8382 \text{ MSH}$  (covering 1.67 % of the visible disk) and  $c = 0.25$ , we obtain  $\Delta \text{TSI}/\text{TSI} = 1.05 \%$ . If we assume a hypothetical extreme case of  $S_{\text{hs}} = 13770 \text{ MSH}$  discussed above (covering 2.7 % of the visible disk), we obtain  $\Delta \text{TSI}/\text{TSI} = 1.7 \%$ .

The reasons why we revisited the case of  $(a, b) = (0.3, 4.0)$  is, on the one hand, to show that this parameter setting leads to overestimated summed total areas of sunspots. On the other hand it is important to remember that the two simulations in Figure 12 are based on the same flux emergence rates, or the same strength of dynamo action. Sunspots live longer for the setting of  $(a, b) = (0.3, 4.0)$  than the case of  $(a, b) = (0.3, 20.0)$  by about a factor of 5, meaning that the former case represents a situation of lower diffusion of sunspot magnetic flux, or possibly weaker surface turbulent convection.

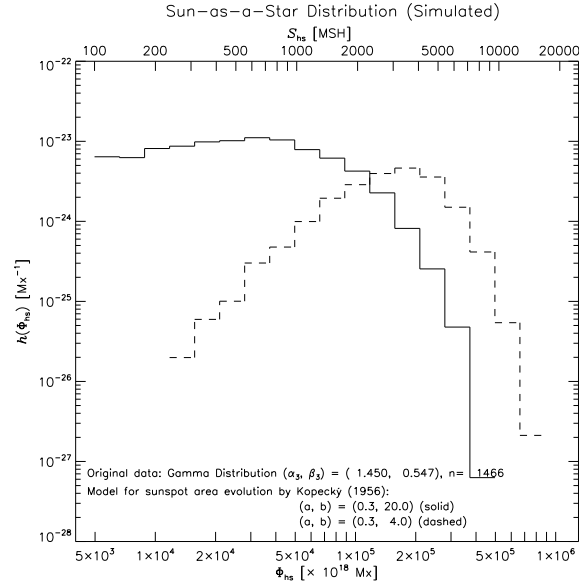


**Figure 12.** The histograms of the probability distribution function  $h(\Phi_{\text{hs}})$  of magnetic flux summed over the observed area, derived from a gamma distribution with  $\alpha_3 = 1.450$  and  $\beta_3 = 0.547$  combined with the sunspot area evolution models of Figure 8. The histogram with a solid line represents the case of our standard setting,  $(a, b) = (0.3, 20.0)$ . The dashed line shows a case of enhanced lifetimes of sunspots,  $(a, b) = (0.3, 4.0)$ , which corresponds to the area-lifetime relation suggested by [Gnevyshev \(1938\)](#) for smaller ( $< 400 \text{ MSH}$ ) sunspots.

## 7. SUMMARY AND DISCUSSION

We have investigated the probability distributions of sunspot areas  $S_{\text{md}} \geq 500$  MSH by using the data from RGO (1987 April – 1976) and USAF/NOAA (1977–2020). Recurrent regions were only counted once at their maximum area development. The data scale of NOAA was adjusted to the scale of RGO by Equation (2), and the sunspot areas were converted to the magnetic flux contents of active regions by Equation (1). We obtained a sample of 2995 regions covering 146.7 years.

The data were fitted by a power-law distribution and four two-parameter distributions (tapered power-law, gamma, lognormal, and Weibull distributions). The parameter values were obtained by the MLE method or by minimizing the revised Kolmogorov-Smirnov metric (KSr, Equation (B37)). Superiority of one model over the other was assessed by the AIC values. The acceptance or rejection of a specific model was assessed by the conventional Kolmogorov-Smirnov (KS) test, or by using KSr and its P-values (probability of realization).

The power-law model was unfavorable compared to the four models in terms of AIC, and was not acceptable by the classical KS test. Among the two-parameter models, the lognormal and Weibull distributions performed well, but their behavior extended to smaller regions ( $S \ll 500$  MSH) did not connect to the previously published results. Therefore, our choices were tapered power-law and gamma distributions. The latter was more favorable considering its consistent sign of curvature of the PDF (Appendix A.4, Figure 13). We also preferred the model determined by KSr=min than the MLE solution; the former directly minimized the deviation of the model CCDF from the observed CCDF, with more weight on the tail of the distribution.

The power-law portion of the tapered power-law and gamma distributions was found to be characterized by its power exponent 1.35–1.9. This was smoothly connected to the power-law distribution of exponent 2 for smaller active regions obtained by Harvey & Zwaan (1993). Modern observations on ephemeral regions and smaller flux concentrations by Hagenaar et al. (2003) and Thornton & Parnell (2011) implied an exponential decline or steeper power law. Although Thornton & Parnell (2011) suggested that all the magnetic structures were fitted by a single power law with an exponent  $\simeq 2.7$ , we argue that this is an extreme conclusion. Large sunspots and ordinary (or small) active regions show the power-law behavior with exponent 1.35–2, and their amplitude changes by a factor of 10 between activity maximum and minimum. Small flux concentrations, whether they follow a steeper power law or exponential decline, do not change significantly between activity maximum and minimum, and we suggest that they give way to the active region population at around  $\Phi_{\text{md}} \simeq 10^{20}$  Mx.

The exponential fall-off of our tapered power-law and gamma distributions were significant, and the expected frequencies of large sunspots (Table 3) were low. The largest sunspot the Sun can generate was estimated to be around  $2 \times 10^4$  MSH. Such an upper limit to exist seems reasonable because the magnetic fields generating sunspots must be amplified within the convection zone, which has a finite size of  $2 \times 10^5$  km (30 % of solar radius).

The effects of time evolution of sunspot areas were estimated by introducing a model by Kopecký (1956). Our model assumed the lifetimes of sunspots roughly one fifth of the empirical relation for lifetimes proposed by Gnevyshev (1938), in order for the flux emergence rates we derived to be consistent with the instantaneous distribution of sunspot areas. Our assumption that the observed maximum area of a region on the visible hemisphere was a reasonable approximation to the true maximum area was confirmed.

By using the same evolution model, we converted the distribution of maximum development areas to the distribution of instantaneous areas, and further derived the Sun-as-a-star distribution functions of total sunspot areas. In the current Sun, the largest total hemispheric areas of sunspots recorded is 8382 MSH, i.e. covering 1.67 % of the visible disk. By artificially increasing the lifetimes of large sunspots, the total area covered by sunspots can be increased, even up to 2.7 % of the solar disk, leading to the modulation in TSI of about 1.7 %.

Recently, [Maehara et al. \(2017\)](#) compared the appearance rates of starspots on slowly rotating solar-type stars and the rates of sunspots and found that the two distributions are not very dissimilar, speculating that the sunspots and larger starspots share a common physical origin. However, in the last 147 years, we observed no sunspots greater than 6132 MSH in area. If the sunspot area distribution were to follow a power law and it were a matter of observation period, perhaps we can find some events of a relevant size by extracting historical records from a period even before that of the RGO data ([Vaquero 2007](#)). Our statistical analysis implies that the probability for the Sun to produce much larger single active region is small; 10000 MSH region every  $3-8 \times 10^4$  years. A similar argument on the hemispheric summed areas of sunspots was not made in this paper because we do not have a model for its distribution function, namely how the distribution decays at large values of summed areas. This will be the task in a future paper.

Our hypothetical simulation runs assuming enhanced lifetime of sunspots (not enhanced generation of large sunspots) showed that the total area of sunspots can reach 2.7 % of the visible disk. The emergence rates of sunspots reflect the process for the solar dynamo to generate magnetic flux, but the lifetime of magnetic structures is controlled by diffusion due to convective eddies. The latter may be an independent process from the dynamo. In the case of the Sun, the diffusive decay of sunspots leads to lifetimes of at most 7 months ([Kopecký 1984](#)). Under which conditions one may have larger starspots (stronger dynamo) or starspots living for many years (reduced diffusion) could be an important issue in understanding the nature of super-large starspots.

The authors would like to thank the referee for useful suggestions that have contributed in improving the data analysis procedures. They also thank Y. Iida for helpful comments. The work of Sakurai was supported by JSPS KAKENHI Grant numbers JP15H05816 and JP20K04033. The work of Toriumi was supported by JSPS KAKENHI Grant numbers JP15H05814, JP16K17671, JP20KK0072, JP21H01124, and JP21H04492, and by the NINS program for cross-disciplinary study (Grant Nos. 01321802 and 01311904) on Turbulence, Transport, and Heating Dynamics in Laboratory and Astrophysical Plasmas: “SoLaBo-X.” .

*Facilities:* SDO(HMI), SOHO(MDI), Hinode(SOT), KPNO

## APPENDIX

### A. PROBABILITY DISTRIBUTION FUNCTIONS

#### A.1. Definitions

To be generic, we will use  $x$  instead of  $\Phi$  for a statistical variable, and consider a semi-infinite range  $x_{\min} \leq x$ . The observed values of  $x$  are indicated by  $x_i$  ( $i = 1, 2, \dots, n$ ). The probability distribution function (PDF) and its complementary cumulative distribution function (CCDF) for flux emergence



rates are denoted by  $P(x)$  and  $F(x)$ , respectively, which are

$$P(x) = -\frac{dF}{dx}, \quad (\text{A1})$$

$$F(x) = \int_x^\infty P(x') dx', \quad (\text{A2})$$

and

$$F(x_{\min}) = \int_{x_{\min}}^\infty P(x) dx = 1. \quad (\text{A3})$$

The observed CCDF ( $F_{\text{obs}}$ ) is defined as an aggregate of step functions,

$$F_{\text{obs}}(x) = (\text{number of data with } x_i \geq x)/n. \quad (\text{A4})$$

At  $x = x_i$ ,  $F_{\text{obs}}(x)$  jumps from  $i/n$  to  $(i-1)/n$ , and  $F_{\text{obs}}(x_i) = i/n$  because of the “ $\geq$ ” condition in Equation (A4).

### A.2. Normalization

The emergence rate of regions with maximum-development magnetic flux  $\Phi_{\text{md}}$  is given by Equation (3),

$$f(\Phi_{\text{md}}) = -\frac{N_s}{AT} \frac{dF(\Phi_{\text{md}})}{d\Phi_{\text{md}}} \quad (\text{A5})$$

(Figures 3, 4, 5, 6, 7, and 9). Here  $T = 5.36 \times 10^4$  days,  $A = 6.2 \times 10^6 \text{Mm}^2$  is the full-Sun area.

For instantaneous distributions of magnetic flux  $\Phi$ , we use  $G(\Phi)$  for CCDF, and the probability distribution  $g(\Phi)$  is given by

$$g(\Phi) = -\frac{N_{\text{rd}}}{AT} \frac{dG(\Phi)}{d\Phi} \quad (\text{A6})$$

(Figure 10). Here  $T = 5.36 \times 10^4$  days,  $A = 3.1 \times 10^6 \text{Mm}^2$  is the area of solar hemisphere.  $N_{\text{rd}}$  is given in Table 4.

For the distributions of summed hemispheric magnetic flux  $\Phi_{\text{hs}}$ , we use  $H(\Phi_{\text{hs}})$  for CCDF and the probability distribution function  $h(\Phi_{\text{hs}})$  is given by

$$h(\Phi_{\text{hs}}) = -\frac{N_d}{T} \frac{dH(\Phi_{\text{hs}})}{d\Phi_{\text{hs}}} \quad (\text{A7})$$

(Figures 11 and 12). Here  $T$  is actually the total number of observations (one observation per day), so that  $T = 5.36 \times 10^4$  observations in Figure 11 for all the cases (maximum, intermediate, minimum, all, and combined). In figure 12,  $T = 1.3 \times 10^4$  observations.  $N_d$  is given in Table 4.

### A.3. Power-Law Distribution

$$F(x) = \left( \frac{x}{x_{\min}} \right)^{-\alpha_1+1} \quad (\alpha_1 > 1), \quad (\text{A8})$$

$$P(x) = \frac{1}{(\alpha_1 - 1)x_{\min}} \left( \frac{x}{x_{\min}} \right)^{-\alpha_1}. \quad (\text{A9})$$

The maximum-likelihood estimator for the power exponent  $\alpha_1$  is given by (e.g., Clauset et al. 2009)

$$\alpha_1 = 1 + \left[ \sum_{i=1}^n \ln \left( \frac{x_i}{x_{\min}} \right) \right]^{-1}. \quad (\text{A10})$$

#### A.4. Tapered Power-Law Distribution

First we define CCDF as (Kagan 2002)

$$F(x) = \left(\frac{x}{x_{\min}}\right)^{-(\alpha_2-1)} \exp\left[-\beta_2 \frac{x - x_{\min}}{x_{\min}}\right] \quad (\alpha_2 > 1, \beta_2 \geq 0), \quad (\text{A11})$$

( $M, M_t, M_{\text{cm}}$ , and  $\beta$  in Kagan (2002) are  $M = x$ ,  $M_t = x_{\min}$ ,  $M_t/M_{\text{cm}} = \beta_2$ , and  $\beta = \alpha_2$  in our notation) which gives the PDF as follows;

$$P(x) = \frac{1}{x_{\min}} \exp\left[-\beta_2 \frac{x - x_{\min}}{x_{\min}}\right] \left[ \frac{1}{\alpha_2 - 1} \left(\frac{x}{x_{\min}}\right)^{-\alpha_2} + \beta_2 \left(\frac{x}{x_{\min}}\right)^{-(\alpha_2-1)} \right]. \quad (\text{A12})$$

The MLE for parameters  $\alpha_2$  and  $\beta_2$  are given by (Kagan & Schoenberg 2001; Vere-Jones et al. 2001)

$$\beta_2 = \left[ n - (\alpha_2 - 1) \sum_{i=1}^n \ln\left(\frac{x_i}{x_{\min}}\right) \right] \left[ \sum_{i=1}^n \frac{x_i - x_{\min}}{x_{\min}} \right]^{-1}, \quad (\text{A13})$$

$$\sum_{i=1}^n \left[ \alpha_2 - 1 + \beta_2 \frac{x_i}{x_{\min}} \right]^{-1} = \sum_{i=1}^n \ln \frac{x_i}{x_{\min}}. \quad (\text{A14})$$

Equation (A14) must be solved numerically for  $\alpha_2$ .

Equation (A12) indicates that the PDF contains two power-law components with exponents  $\alpha_2$  and  $\alpha_2 - 1$ , the former being the dominant component for small  $x$ . We can show that

$$\frac{d^2 \ln P}{d(\ln x)^2} = -\frac{\beta_2 x}{x_{\min}} \left[ 1 - \frac{\alpha_2 - 1}{(\alpha_2 - 1 + \beta_2 x/x_{\min})^2} \right]. \quad (\text{A15})$$

The sign of this quantity is distributed as in Figure 13a. For  $\alpha_2 > 2$ ,  $d^2 \ln P/d(\ln x)^2$  is always negative, and the slope of  $\ln P$  as a function of  $\ln x$  monotonically steepens as  $x$  increases. If  $1 < \alpha_2 < 2$ ,  $d^2 \ln P/d(\ln x)^2$  changes sign at  $\beta_2 x/x_{\min} = \sqrt{\alpha_2 - 1} - (\alpha_2 - 1)$ , namely the slope of  $\ln P$  as a function of  $\ln x$  first flattens and then steepens as  $x$  increases. This “reversed curvature” is conspicuous if  $\alpha_2$  is close to 1 (Figure 13b), and could be an undesirable feature of this distribution function if the inflection point appears in the fitting range ( $x_{\min} < x$ ), or if we extend the distribution down below  $x_{\min}$ .

#### A.5. Truncated Gamma Distribution

We first define PDF as (Kagan 2002)

$$P(x) = C \left(\frac{x}{x_{\min}}\right)^{-\alpha_3} \exp\left[-\beta_3 \frac{x}{x_{\min}}\right] \quad (\alpha_3 > 1, \beta_3 \geq 0), \quad (\text{A16})$$

where  $C$  is fixed from the normalization condition as

$$C = \frac{\beta_3^{1-\alpha_3}}{x_{\min} \Gamma(1 - \alpha_3, \beta_3)} \quad (\text{A17})$$

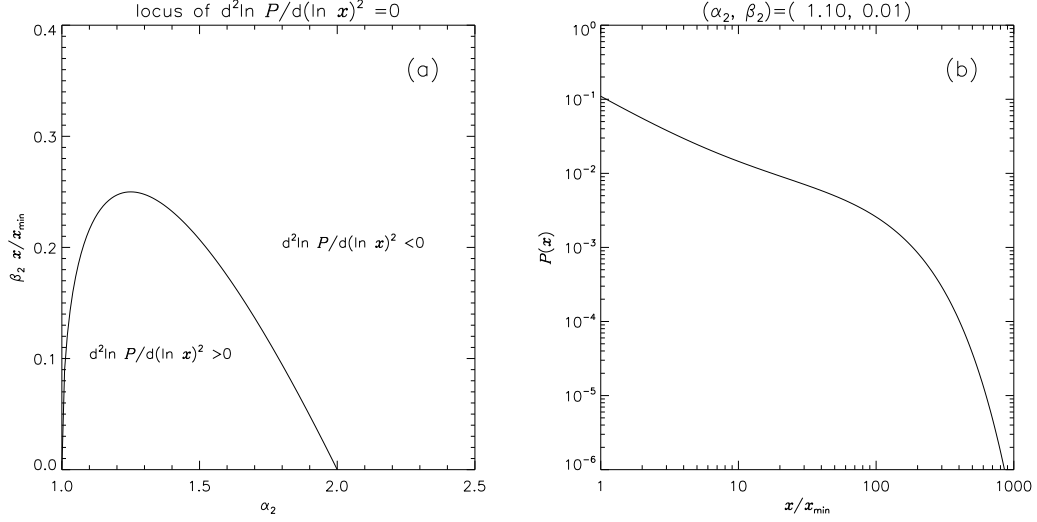


**Figure 13.** (a) The locus of  $d^2 \ln P / d(\ln x)^2 = 0$ . In the area above this curve, the slope of  $\ln P$  as a function of  $\ln x$  monotonically steepens as  $x$  increases. (b) An example of  $P(x)$  for  $\alpha_2 = 1.1$  and  $\beta_2 = 0.01$ . The slope is not monotonic, and an inflection point appears.

and  $\Gamma$  stands for the incomplete gamma function defined by

$$\Gamma(a, y) = \int_y^\infty t^{a-1} e^{-t} dt. \quad (\text{A18})$$

If  $\alpha_3 < 0$  (which is more common cases in application),  $P(x)$  can be defined down to  $x = 0$ . Here we consider the case  $\alpha_3 > 1$  so that  $x$  must be bounded from below as  $x \geq x_{\min}$ , hence the name "truncated gamma distribution." CCDF is given by

$$F(x) = \frac{\Gamma(1 - \alpha_3, \beta_3 x / x_{\min})}{\Gamma(1 - \alpha_3, \beta_3)}. \quad (\text{A19})$$

In order for  $\Gamma$ -function not to diverge at  $\beta_3 \rightarrow 0$  and  $\alpha_3 > 1$ , a recurrence formula

$$\Gamma(a + 1, y) = a\Gamma(a, y) + y^a e^{-y} \quad (\text{A20})$$

is used to rewrite  $F(x)$  as

$$F(x) = \frac{\Gamma(3 - \alpha_3, \eta) - \eta^{2-\alpha_3} e^{-\eta} - (2 - \alpha_3) \eta_3^{1-\alpha_3} e^{-\eta}}{\Gamma(3 - \alpha_3, \beta_3) - \beta_3^{2-\alpha_3} e^{-\beta_3} - (2 - \alpha_3) \beta_3^{1-\alpha_3} e^{-\beta_3}} \quad (\eta = \beta_3 x / x_{\min}), \quad (\text{A21})$$

which can be safely used for  $1 < \alpha_3 < 3$ .

To obtain the MLE solutions for  $\alpha_3$  and  $\beta_3$ , the log-likelihood LLH,

$$\text{LLH} = n \ln C - \alpha_3 \sum_{i=1}^n \ln \frac{x_i}{x_{\min}} - \beta_3 \sum_{i=1}^n \frac{x_i - x_{\min}}{x_{\min}} \quad (\text{A22})$$

is usually maximized for both  $\alpha_3$  and  $\beta_3$  numerically (Johnson et al. 2011). Here we use the condition  $\partial \text{LLH} / \partial \beta_3 = 0$  explicitly, i.e.

$$\ln \Gamma(1 - \alpha_3, \beta_3) = -\alpha_3 \ln \beta_3 - \beta_3 - \ln \left[ \frac{\alpha_3 - 1}{\beta_3} + \frac{1}{n} \sum_{i=1}^n \frac{x_i}{x_{\min}} \right] \quad (\text{A23})$$

which gives  $\beta_3$  if  $\alpha_3$  is specified. Therefore, LLH is maximized for  $\alpha_3$  to obtain the MLE solution.

#### A.6. Truncated Lognormal Distribution

We first define PDF as

$$P(x) = \frac{C}{\sqrt{2\pi}\sigma x} \exp \left[ -\frac{\{\ln(x/x_{\min}) - \mu\}^2}{2\sigma^2} \right] \quad (\text{A24})$$

where  $C$  is fixed from the normalization condition as

$$C = 2 \left[ 1 - \operatorname{erf} \left( -\frac{\mu}{\sqrt{2}\sigma} \right) \right]^{-1} \quad (\text{A25})$$

and  $\operatorname{erf}$  stands for the error function defined by

$$\operatorname{erf}(y) = \frac{2}{\sqrt{\pi}} \int_0^y e^{-t^2} dt. \quad (\text{A26})$$

The peak of  $P$  is at  $x_{\min} \exp(\mu - \sigma^2)$ . The lognormal distributions can generally be defined down to  $x = 0$ , and under such cases the mean and the dispersion are given by  $x_{\min} \exp(\mu + \sigma^2/2)$  and  $x_{\min}^2 \exp(2\mu + \sigma^2)[\exp(\sigma^2) - 1]$ . In our case we truncate the distribution at  $x = x_{\min}$ , so that the mean and the dispersion are not given by these formula.

CCDF is given by

$$F(x) = \left[ 1 - \operatorname{erf} \left( \frac{\ln(x/x_{\min}) - \mu}{\sqrt{2}\sigma} \right) \right] \left[ 1 - \operatorname{erf} \left( \frac{-\mu}{\sqrt{2}\sigma} \right) \right]^{-1}. \quad (\text{A27})$$

By introducing  $\zeta = \mu/\sigma$ , the MLE solution is given by (Crow & Shimizu 2020)

$$\sigma = \frac{1}{n} \sum_{i=1}^n \ln \frac{x_i}{x_{\min}} \left[ \zeta + \sqrt{\frac{2}{\pi}} \frac{e^{-\zeta^2/2}}{1 - \operatorname{erf}(-\zeta/\sqrt{2})} \right]^{-1} \quad (\text{A28})$$

and

$$1 - \sqrt{\frac{2}{\pi}} \zeta \frac{e^{-\zeta^2/2}}{1 - \operatorname{erf}(-\zeta/\sqrt{2})} = \frac{1}{n} \sum_{i=1}^n \left[ \frac{1}{\sigma} \ln \left( \frac{x_i}{x_{\min}} \right) - \zeta \right]^2. \quad (\text{A29})$$

Equation (A29) must be solved numerically for  $\zeta$ .

#### A.7. Truncated Weibull Distribution

CCDF and PDF are given by (Weibull 1939)

$$F(x) = \exp \left[ -\beta_5 \left( \frac{x}{x_{\min}} \right)^k + \beta_5 \right] \quad (k > 0, \beta_5 > 0) \quad (\text{A30})$$

and

$$P(x) = \frac{\beta_5 k}{x_{\min}} \left( \frac{x}{x_{\min}} \right)^{k-1} \exp \left[ -\beta_5 \left( \frac{x}{x_{\min}} \right)^k + \beta_5 \right]. \quad (\text{A31})$$

If  $k \geq 1$ ,  $P(x)$  can be defined down to  $x = 0$ . Here we consider the case  $k < 1$ , so that the equations above are here modified to include the truncation at  $x = x_{\min}$ . The MLE solutions are given by (Wingo 1989)

$$\beta_5 = \left[ \frac{1}{n} \sum_{i=1}^n \left( \frac{x_i}{x_{\min}} \right)^k - 1 \right]^{-1} \quad (\text{A32})$$

and

$$\frac{n}{k} + \sum_{i=1}^n \ln \frac{x_i}{x_{\min}} \left[ 1 - \beta_5 \left( \frac{x_i}{x_{\min}} \right)^k \right] = 0. \quad (\text{A33})$$

Equation (A33) must be solved numerically for  $k$ .

The behavior of  $P$  near  $x \simeq x_{\min}$  is

$$P(x) \simeq \frac{\beta_5 k}{x_{\min}} \left[ 1 - \frac{x - x_{\min}}{x_{\min}} (1 - k + \beta_5 k) \right], \quad (\text{A34})$$

so that the slope in the  $\ln P$  vs.  $\ln x$  plot at  $x = x_{\min}$  is  $d \ln P / d \ln x = -(1 - k + \beta_5 k)$ .

The behavior of  $P$  at  $x \simeq 0$  is

$$P(x) \simeq \frac{\beta_5 k}{x_{\min}} \left( \frac{x}{x_{\min}} \right)^{-(1-k)} \exp(\beta_5) \quad (\text{A35})$$

so that the distribution approaches a power law with exponent  $1 - k$ .

## B. EVALUATION METRICS

The goodness-of-fit metrics measure the distance between the theoretical and observed CCDFs. In this paper we use the Kolmogorov-Smirnov metric (KS) and its variant, KSr.

### B.1. Kolmogorov-Smirnov Metric

The KS metric is defined as (Stephens 1970, 2016)

$$\text{KS} = \max_{1 \leq i \leq n} \left( \frac{n+1-i}{n} - F(x_i), F(x_i) - \frac{n-i}{n} \right). \quad (\text{B36})$$

For large-enough  $n$ , the probability of obtaining  $\sqrt{n}$  KS larger than a specified value is given by the so-called Kolmogorov-Smirnov function with relatively weak dependence on  $n$ , regardless of the form of CCDF. We used the method proposed by Simard & L'Ecuyer (2011) to calculate the Kolmogorov-Smirnov function.

### B.2. Modified Kolmogorov-Smirnov Metric

Since the observed and theoretical CCDFs match at  $x \simeq x_{\min}$  and  $x \rightarrow \infty$  by definition, the data points in these regions have less contributions to the KS metric compared to mid data points. As a matter of fact, the contributions scale as  $\sqrt{F(1-F)}$  (Anderson & Darling 1952). Therefore, one can obtain more uniform contributions from all the data by dividing the difference by  $1/\sqrt{F(1-F)}$  (Anderson & Darling 1952; Clauset et al. 2009). In this paper we adopt

$$\text{KSr} = \max_{1 \leq i \leq n} \left( \frac{n+1-i}{n} - F(x_i), F(x_i) - \frac{n-i}{n} \right) / \sqrt{F(x_i)}, \quad (\text{B37})$$

to emphasize the tail portion only. A mismatching near  $x \simeq x_{\min}$  may occur from physical (e.g. limitation in detecting small sunspots, which is very unlikely in the present study because 500 MSH sunspots are big) or technical reasons. Therefore, we do not want to amplify it.

### C. COMPARISON WITH PUBLISHED DATA

Here we will summarize the flux emergence rates [Equation (3)] given in the literature and how they were converted and plotted in Figure 7 in units of  $\text{Mx}^{-1} \text{Mm}^{-2} \text{d}^{-1}$ . The values of  $n$ ,  $A$ , and  $T$  differ in individual data sources.

#### C.1. *Thornton & Parnell (2011)*

*Thornton & Parnell (2011)* analyzed the emergence rates of small-scale magnetic field patches using the data from Hinode/SOT and obtained a formula extending all the way up to the active-region scales,

$$f_{\text{ThP}} = \frac{n_0}{\Phi_0} \left( \frac{\Phi}{\Phi_0} \right)^{-\alpha} \quad [\text{Mx}^{-1} \text{cm}^{-2} \text{day}^{-1}] \quad (\text{C38})$$

where  $n_0 = 3.14 \times 10^{-14} \text{cm}^{-2} \text{day}^{-1}$ ,  $\Phi_0 = 1.0 \times 10^{16} \text{Mx}$ , and  $\alpha = -2.69$ . In Figure (7) is plotted  $\tilde{f}_{\text{ThP}} = f_{\text{ThP}} \times 10^{16}$ , the last factor is  $(\text{Mm}/\text{cm})^2$ .

Figure 5 of *Thornton & Parnell (2011)* were also copied to Figure 7 using geometrical approximations to their curves.

#### C.2. *Harvey & Zwaan (1993), Schrijver & Harvey (1994)*

*Harvey & Zwaan (1993)* derived the emergence rates of bipolar active regions using the data obtained at NSO Kitt Peak (*Livingston et al. 1976*). The data were taken on 739 days nearly uniformly distributed from 1975 to 1986. Table 6 reproduces the data give in their Table 1 before various corrections (data gaps, etc.) were applied. We have converted the area data  $A_j$  and  $\Delta A_j$  in square degrees (sq. deg. =  $1.48 \times 10^{18} \text{cm}^2$ ) to magnetic flux as

$$\Phi_j [\text{Mx}] = 150 \times A_j \times 1.48 \times 10^{18}, \quad (\text{C39})$$

$$\Delta \Phi_j [\text{Mx}] = 150 \times \Delta A_j \times 1.48 \times 10^{18}. \quad (\text{C40})$$

The conversion factor  $150 \text{Mx cm}^{-2}$  (or mean field strength) was taken from *Schrijver & Harvey (1994)*, who suggested 136 and 153 derived from different methods. The histogram in Figure 7 shows the counts  $N_j/(\tau_{\text{obs}} \Delta \Phi_j S_h)$  where  $\tau_{\text{obs}} = 739 \text{d}$  and  $S_h = 3.04 \times 10^6 [\text{Mm}^2]$  is the area of solar hemisphere.

*Schrijver & Harvey (1994)* reported that the area distribution  $N_j(A_j)$  is fitted by a power law with exponent  $p = 2$ , namely

$$\tilde{N}_j(A_j) = a^* A_j^{-p}, \quad (\text{C41})$$

with amplitudes  $a^* = 1.23$  for activity minima and  $a^* = 10$  for activity maxima. This range of values is shown in Figure 7 as two parallel lines, after the following conversion

$$\tilde{N}(\Phi_j) = a^* A_j^{-p} / [150 \times (1.48 \times 10^{18}) \times S_h]. \quad (\text{C42})$$

#### C.3. *Hagenaar et al. (2003)*

*Hagenaar et al. (2003)* investigated the emergence rates of small-scale bipolar magnetic field patches (ephemeral regions) using the data from SOHO/MDI. The data were taken between 1996 and 2001.



**Table 6.** Data reproduced from [Harvey & Zwaan \(1993\)](#). Here  $j$  represents the bin number,  $A_j$  and  $\Delta A_j$  represent the area and bin width in square degrees, and  $N_j$  represents the number of regions of the  $j$ -th bin.

$j$	1	2	3	4	5	6	7	8	9	10	11
$A_j$	2.90	3.93	4.95	5.95	6.99	8.00	8.91	9.92	11.34	13.13	15.47
$\Delta A_j$	1.0	1.0	1.0	1.0	1.0	1.0	1.0	1.0	2.0	2.0	2.0
$N_j$	313	155	77	65	44	32	30	24	56	26	27
$j$	12	13	14	15	16	17	18	19	20	21	22
$A_j$	17.29	19.32	22.63	26.15	30.10	35.89	44.07	51.66	60.70	68.50	73.30
$\Delta A_j$	2.0	2.0	4.0	4.0	4.0	8.0	8.0	8.0	8.0	8.0	8.0
$N_j$	30	17	23	17	9	23	3	5	1	0	1

In their Figure 11 they presented the flux emergence rates in number of regions per day per  $10^{18}$  Mx bin over the whole solar surface for the data of 1997 October and 2000 August as

$$f_H = S_{\text{cm}}(28.4 \times 10^{-20}) \exp(-\Phi/(10^{18}[\text{Mx}] \times 5.5f_c)) \quad (1997 \text{ October}), \quad (\text{C43})$$

$$f_H = S_{\text{cm}}(21.1 \times 10^{-20}) \exp(-\Phi/(10^{18}[\text{Mx}] \times 5.2f_c)) \quad (2000 \text{ August}). \quad (\text{C44})$$

Here  $1 \times 10^{18} \text{ Mx} < \Phi \lesssim 6 \times 10^{18} \text{ Mx}$ ,  $S_{\text{cm}} = 6.1 \times 10^{22}$  is the whole solar area in  $\text{cm}^2$ , and  $f_c = 1.6$  is a conversion factor to put the MDI field strength to the scale of NSO Kitt Peak. In Figure 7 these were converted to

$$\tilde{f}_H = f_H/(1.0 \times 10^{18}[\text{Mx}] \times S_{\text{Mm}}) \quad (\text{C45})$$

where  $S_{\text{Mm}} = 6.1 \times 10^6$  is the whole solar area in  $\text{Mm}^2$ .

#### C.4. *Baumann & Solanki (2005)*

[Baumann & Solanki \(2005\)](#) presented the lognormal distributions fitted to the RGO sunspot area data. They adopted the form

$$\ln \left( \frac{dN}{dA} \right) = -\frac{(\ln A - \ln \langle A \rangle)^2}{2 \ln \sigma_A} + \ln \left( \frac{dN}{dA} \right)_{\text{max}} \quad (\text{C46})$$

with the normalization

$$\int_{A_{\text{min}}}^{\infty} \frac{dN}{dA} dA = 1 \quad (\text{C47})$$

and parameter values  $A_{\text{min}} = 60 \text{ MSH}$ ,  $\langle A \rangle = 62.2 \text{ MSH}$ , and  $\sigma_A = 2.45 \text{ MSH}$ . These are converted to our standard form [Cf. Equation (A24)]

$$P_B(A) = \frac{\tilde{C}}{\sqrt{2\pi}\tilde{\sigma}A} \exp \left[ -\frac{\{\ln(A/A_{\text{min}}) - \tilde{\mu}\}^2}{2\tilde{\sigma}^2} \right] \quad (\text{C48})$$

by taking  $\tilde{\mu} = \ln \langle A \rangle + \ln \sigma_A$ ,  $\tilde{\sigma} = \sqrt{\ln \sigma_A}$ . Then, by applying Equation (1), we obtain Equation (A24) with  $\mu = \tilde{\mu}p$ ,  $\sigma = \tilde{\sigma}p$  ( $p = 1.02$ ).

C.5. *Gopalswamy (2018)*

*Gopalswamy (2018)* made a general study of the applicability of Weibull distribution to various indices of solar activity. He used the formula for CCDF, represented by  $y$ , as

$$\log y = a \left[ 1 - \exp \left( -\frac{\gamma - \log x}{\eta} \right) \right]. \quad (\text{C49})$$

When  $x$  is the sunspot area in MSH observed at RGO and NOAA (1874 May to 2016 December) and  $y$  is the number of regions with area  $> x$ , *Gopalswamy (2018)* gave the parameter values  $a = 2.5$ ,  $\gamma = 3.3$ , and  $\eta = 0.8$ . This should match our representation for CCDF,

$$F_G = n \exp \left[ \beta - \beta \left( \frac{x}{x_{\min}} \right)^k \right] \quad (x \geq x_{\min}). \quad (\text{C50})$$

Here we adopt the un-normalized CCDF with a factor  $n = 41433$  representing the total number of data. The parameters are related as follows.

$$k = [\eta \ln 10]^{-1}, \quad (\text{C51})$$

$$\beta = a \ln 10 - \ln n, \quad (\text{C52})$$

$$x_{\min} = 10^\gamma \left( 1 - \frac{1}{a} \ln n \right)^{1/k}. \quad (\text{C53})$$

After converting sunspot area  $x$  to magnetic flux  $\Phi$  by Equation (1), and using  $t_{\text{obs}} = 5.21 \times 10^4$  d (from 1874 May to 2014 December) and  $S_{\text{obs}} = 6.1 \times 10^6$  (the whole solar area in  $\text{Mm}^2$ ), a Weibull PDF multiplied by  $n/(t_{\text{obs}} S_{\text{obs}})$  is plotted in Figure 7. We assume that *Gopalswamy (2018)* did not make particular considerations on recurrent regions, so that some mismatching is anticipated.

## REFERENCES

- |   |  |
|---|--|
| <p>Akaike, H. 1974, IEEE Transactions on Automatic Control, 19, 716</p> <p>Anderson, T. W., &amp; Darling, D. A. 1952, Annals of Mathematical Statistics, 23, 193</p> <p>Antalova, A. &amp; Macura, R. 1986, Contributions of the Astronomical Observatory Skalnaté Pleso, 14, 163</p> <p>Arge, C. N., Hildner, E., Pizzo, V. J., et al. 2002, J. Geophys. Res., 107, 1319</p> <p>Balmaceda, L. A., Solanki, S. K., Krivova, N. A., &amp; Foster, S. 2009, Journal of Geophysical Research (Space Physics), 114, 7104</p> <p>Baumann, I., &amp; Solanki, S. K. 2005, A&amp;A, 443, 1061</p> <p>Berdugina, S. V. 2005, Living Reviews in Solar Physics, 2, 8</p> | <p>Bobra, M. G., Sun, X., Hoeksema, J. T., et al. 2014, SoPh, 289, 3549</p> <p>Bogdan, T. J., Gilman, P. A., Lerche, I., et al. 1988, ApJ, 327, 451</p> <p>Buehler, D., Lagg, A., &amp; Solanki, S. K. 2013, A&amp;A, 555, A33</p> <p>Burnham, K. P., &amp; Anderson, D. R. 2002, Model Selection and Multimodel Inference, Springer, New York, p.210, p.279</p> <p>Burnham, K. P., Anderson, D. R., &amp; Huyvaert, K. P. 2011, Behavioral Ecology and Sociobiology, 65, 23</p> <p>Cattaneo, F. 1999, ApJL, 515, L39</p> <p>Christie, W. H. M. 1907, Photo-Heliographic Results 1874 to 1885 Being Supplementary Results from Photographs of the Sun (Bellevue, Edinburgh: Neill &amp; Co.)</p> |
|---|--|

- Clauset, A., Shalizi, C. R., & Newman, M. E. J. 2009, *SIAM Review*, 51, 661
- Criscuoli, S., Romano, P., Giorgi, F., & Zuccarello, F. 2009, *A&A*, 506, 1429
- Crow, E.L., & Shimizu, K. 2020, *Lognormal Distributions* (Boca Raton, FL: CRC Press)
- Deming, W. E. 1943, *Statistical Adjustment of Data*. John Wiley and Sons, New York, p.184
- Efron, B., & Tibshirani, R. J. *An Introduction to the Bootstrap*, Springer Science+Business Media, Dordrecht, p.306
- Fligge, M., & Solanki, S. K. 1997, *SoPh*, 173, 427
- Foukal, P. 2014, *SoPh*, 289, 1517
- Gnevyshev, M. N. 1938, *Pulkovo Obs. Circ.*, 24, 37
- Gopalswamy, N. 2018, in *Extreme Events in Geospace*, ed. N. Buzulukova (Amsterdam: Elsevier), 37–63
- Harvey, K. L., & Zwaan, C. 1993, *SoPh*, 148, 85
- Hagenaar, H. J., Schrijver, C. J., & Title, A. M. 2003, *ApJ*, 584, 1107
- Hathaway, D. H. 2015, *Living Reviews in Solar Physics*, 12, 4
- Hathaway, D. H., & Choudhary, D. P. 2008, *SoPh*, 250, 269
- Hathaway, D. H., Wilson, R. M., & Reichmann, E. J. 2002, *SoPh*, 211, 357
- Howard, R. F. 1992, *SoPh*, 137, 51
- Hudson, H. S., Silva, S., Woodard, M., et al. 1982, *SoPh*, 76, 211
- Johnson, N. L., Kotz, S., & Balakrishnan, N. 1994, *Continuous Univariate Distributions*, Vol.1, 2nd Ed., Wiley-Interscience, New York, p.575
- Johnson, R. W., Kliche, D. V., & Smith, P. L. 2011, *J. Appl. Meteor. Clim.*, 50, 296
- Kagan, Y. Y., & Schoenberg, F. 2001, *J. Appl. Probab.*, 38A, 158
- Kagan, Y. Y. 2002, *Geophysical Journal International*, 148, 520
- Kopecký, M. 1956, *Bulletin of the Astronomical Institutes of Czechoslovakia*, 7, 116
- Kopecký, M. 1953, *Bulletin of the Astronomical Institutes of Czechoslovakia*, 4, 1
- Kopecky, M. 1984, *SoPh*, 93, 181
- Kopp, G. 2021, *SoPh*, 296, 133
- Livingston, W. C., Harvey, J., Slaughter, C., et al. 1976, *ApOpt*, 15, 40
- Maehara, H., Notsu, Y., Notsu, S., et al. 2017, *PASJ*, 69, 41
- Maehara, H., Shibayama, T., Notsu, S., et al. 2012, *Nature*, 485, 478
- Mandal, S., Krivova, N. A., Solanki, S. K., et al. *A&A*, 640, A78
- Maunder, A. S. D. 1909, *Catalogue of Recurrent Groups of Sun Spots for the Years 1874 to 1906* (Bellevue, Edinburgh: Neill & Co.)
- Muñoz-Jaramillo, A., Senkpeil, R. R., Windmueller, J. C., et al. 2015, *ApJ*, 800, 48
- Nagovitsyn, Y. A., Ivanov, V. G., & Skorbezh, N. N. 2019, *Astronomy Letters*, 45, 396
- Notsu, Y., Honda, S., Maehara, H., et al. 2015, *PASJ*, 67, 33
- Notsu, Y., Shibayama, T., Maehara, H., et al. 2013, *ApJ*, 771, 127
- Parker, E. N. 1955, *ApJ*, 121, 491
- Pesnell, W. D., Thompson, B. J., & Chamberlin, P. C. 2012, *SoPh*, 275, 3
- Press, W. H., Flannery, B. P., Teukolsky, S. A., Vetterling, W. T. 1992, *Numerical Recipes in FORTRAN 77: The Art of Scientific Computing*, Volume 1 of Fortran Numerical Recipes (Cambridge: Cambridge University Press), pp.660-664
- Priest, E. R., & Forbes, T. G. 2002, *A&A Rv*, 10, 313
- Sammis, I., Tang, F., & Zirin, H. 2000, *ApJ*, 540, 583
- Schaefer, B. E., King, J. R., & Deliyannis, C. P. 2000, *ApJ*, 529, 1026
- Scherrer, P. H., Bogart, R. S., Bush, R. I., et al. 1995, *SoPh*, 162, 129
- Scherrer, P. H., Schou, J., Bush, R. I., et al. 2012, *SoPh*, 275, 207
- Schou, J., Scherrer, P. H., Bush, R. I. et al. 2012, *SoPh*, 275, 229
- Schrijver, C. J., & Harvey, K. L. 1994, *SoPh*, 150, 1
- Serra, I. & Corral, Á. 2017, *Scientific Reports*, 7, 40045
- Shibata, K., & Magara, T. 2011, *Living Reviews in Solar Physics*, 8, 6
- Simard, R., & L'Ecuyer, P. 2011, *J. Stat. Software*, 39, issue 11
- Smyrli, A., Zuccarello, F., Romano, P., et al. 2010, *A&A*, 521, A56
- Solanki, S. K. 2003, *A&A Rv*, 11, 153

- Spencer Jones, H. 1955, Sunspot and Geomagnetic-Storm Data Derived from Greenwich Observations, 1874-1954 (London: Her Majesty's Stationery Office)
- Spruit, H. C. 1977, *SoPh*, 55, 3
- Stephens, M. A. 1970, *J. Roy. Stat. Soc. B*, 32, 115.
- Stephens, M. A. in *Wiley StatsRef: Statistics Reference Online* (Hoboken, NJ: Wiley)
- Strassmeier, K. G. 1999, *A&A*, 347, 225
- Strassmeier, K. G. 2009, *A&A Rv*, 17, 251
- Sun, X., Bobra, M. G., Hoeksema, J. T., et al. 2015, *ApJL*, 804, L28
- Thornton, L. M., & Parnell, C. E. 2011, *SoPh*, 269, 13
- Tian, L., & Alexander, D. 2008, *ApJ*, 673, 532
- Toriumi, S., Schrijver, C. J., Harra, L. K., Hudson, H., & Nagashima, K. 2017, *ApJ*, 834, 56
- Toriumi, S. & Wang, H. 2019, *Living Reviews in Solar Physics*, 16, 3
- Tsuneta, S., Ichimoto, K., Katsukawa, Y., et al. 2008, *SoPh*, 249, 167
- Utsu, T. 1999, *Pure and Applied Geophysics*, 155, 509
- van Driel-Gesztelyi, L., & Green, L. M. 2015, *Living Reviews in Solar Physics*, 12, 1
- Vaquero, J. M. 2007, *Advances in Space Research*, 40, 929
- Vere-Jones, D., Robinson, R., & Yang, W. 2001, *Geophysical Journal International*, 144, 517
- Weibull, W. 1939, *Proceedings No.153*, Royal Swedish Institute for Engineering Research
- Wingo, D. R. 1989, *Statistical Papers*, 30, 39
- Zhang, J., Wang, Y., & Liu, Y. 2010, *ApJ*, 723, 1006
- Zwaan, C. 1987, *ARA&A*, 25, 83